THE UNIVERSITY OF CHICAGO

FAST CONTROL OF LOW-FREQUENCY FLUXONIUM QUBITS

A DISSERTATION SUBMITTED TO
THE FACULTY OF THE DIVISION OF THE PHYSICAL SCIENCES
IN CANDIDACY FOR THE DEGREE OF
DOCTOR OF PHILOSOPHY

DEPARTMENT OF PHYSICS

BY
HELIN ZHANG

CHICAGO, ILLINOIS
AUGUST 2023

TABLE OF CONTENTS

LIST OF FIGURES

LIST OF TABLES

ACKNOWLEDGMENTS

There are many people that helped me along my PhD journey, and it is impossible to thank everyone here. I got an opportunity to learn about quantum computation when I was an undergraduate special student at MIT, and I really appreciate the guide I received there from Prof. Edward Farhi. When I was applying for PhD programs, I was interested in both quantum algorithms and experiments. I had an opportunity to work with Prof. David Schuster, also my PhD advisor shortly after I was admitted to the PhD program of the University of Chicago, and he was the person who lead me onto the path of working as an experimentalist. The discussion with Dave has always been enlightening and fruitful, as there are so many things that I can learn from him. My work on the fluxonium qubit is about exploring new control protocols and designs that could improve its performance, and I can feel that this is the aspect that Dave is extremely good at. He has very strong intuitions and profound knowledge on the research of novel qubits in general, and this has always encouraged me to think more, calculate more, and explore more ideas.

I also would like to thank Prof. Jens Koch from the Northwestern University. We received many helps on the theoretical problems from Jens and his group memebers, and more importantly, we learned a lot from the discussions with him. Jens is very rigorous and careful about the statements in the discussions, and very often demands mathematical proofs for ideas from intuition. This reminds me regularly that I need to write everything down in the language of mathematics, and by doing this I believe that I understand many things in a much better way.

During my PhD I also received great help from many members of the Schuster Lab, including but not limited to Nate Earnest, Yao Lu, Vatsan Chakram, Alex Ma, Tanay Roy, Yuwei Ma and Chunyang Ding. Our theory collaborators from the Koch Lab includes Daniel Weiss, Ziwen Huang, Sai Pavan Chitta and Danyang Chen. I really appreciate the working experience with all the collaborators that we had on this project, and would like

to thank them all. I also would like to thank all the Schuter Lab members that are not mentioned above, since they created a great lab environment which is essential for every project happened in this lab. I am very grateful that I had the opportunity to be part of it, and hope for the future success of all the lab members and collaborators.

ABSTRACT

Large scale quantum processors require high quality qubits and good inter-qubit couplings. Superconducting circuit is one of the most promising platforms for building NISQ era devices and executing error correction protocols due to its high two-qubit gate fidelities and clear path for scaling up. Despite the fast development on superconducting circuits (mostly based on transmon qubits), the two-qubit gate fidelities still need two orders of magnitude improvement to realize quantum error correction for solving real-world problems. The fluxonium qubit, which this thesis will be focusing on, is a very promising candidate due to its long coherence times, large anharmonicity and large parameter space for design diversity. By using low frequency fluxonium qubits, we achieve longer coherence times despite having the same material limitations. In this thesis, we demonstrate fast flux pulses that can finish arbitrary single qubit gates within a qubit Larmor period, while not introducing any DC components to the flux line. We also present the two-qubit gate protocol that works with this scheme, which only takes a few Larmor periods for a $\sqrt{i\text{SWAP}}$ or $\sqrt{b\text{SWAP}}$ gate. We will discuss how the low frequency qubits can have long coherence times and how to operate the qubit despite the thermal heating. We believe that there is a path for fluxoniums to gain a large factor in performance compared to the current transmon systems based on the improved control designs.

CHAPTER 1

INTRODUCTION

It has been over 40 years since Richard Feynman raised the question of simulating quantum physics on a computer, and proposed the idea of a quantum computer. The goal, as Feynman stated, is that "the number of computer elements required to simulate a large physical system is only to be proportional to the space-time volume of the physical system." At that time, Feynman already had the idea that classical computers cannot simulate large scale quantum systems efficiently, and he made this famous conclusion

> Nature isn't classical, dammit, and if you want to make a simulation of Nature, you'd better make it quantum mechanical, and by golly it's a wonderful problem because it doesn't look so easy.

It was soon discovered that quantum computers can solve some classical problems more efficiently than classical computers. Most notably, Peter Shor came up with a quantum algortihm that performs Fourier transform with exponential speedup, and used it to construct an efficient quantum algorithm for factoring large numbers, aka the famous Shor's algorithm. Shor's algorithm demonstrated the power of quantum computing in real-world use cases due to its implications for cryptanalysis. However, many physicists believe that the decoherence process in quantum systems makes the quantum computer very difficult to realize, and it is "the computer scientist's dream [but] the experimenter's nightmare." To address this problem, physicists discovered quantum error correction codes and fault-tolerant methods for performing quantum computations consistently with noisy hardware. The quantum error correction (QEC) codes proposed a way that quantum computers can scale up to large devices and solve problems with real world implications, if the errors from the physical systems are scarce and weakly correlated.

There are many systems in development as candidates for the generic quantum computer. However, all these systems inevitably suffer from the decoherence caused by the coupling to

the environment, and none of them is good enough to execute large scale quantum algorithms to solve important problems currently. Nonetheless, in 2019 the Google AI Quantum group declared the achievement of an important milestone, known as "quantum supremacy" Arute et al. [2019]. The Google group constructed a programmable quantum computer called Sycamore with a two-dimensional array of superconducting circuits fabricated on a small chip. The chip consists of 53 qubits, and they are coupled to their nearest neighbors which enabled two-qubit quantum gates to perform on each pair of neighboring qubits. The Google group could only perform 20 layers of two-qubit gates before the quantum errors (mostly from decoherence) completely destroy the output and generate random answers. At the circuit depth of 20, the probability of getting a correct answser is only around 0.2%, but by repeating the same computation process many times, it is statistically significant compared to the other random answers due to quantum errors. To calculate the same problem that Sycamore did, it would take the most powerful classical supercomputer a few days at least, as the cost of the classical simulation grows exponentially with the number of qubits. This has proved Feynman's initial idea of the necessity to simulate quantum systems with quantum computers, since it would be very far beyond the classical computer's reach if there are more qubits in a quantum system. While the classical computer occupies the equivalent of two tennis courts and consumes megawatts of power, Sycamore is just a single chip nested inside a dilution refrigerator Preskill [2023].

Despite being one of the leading platforms for quantum computing, the superconducting qubits still need significant improvements to realize quantum error correction. Currently the most promising error correction code for superconducting qubits is the surface code Fowler et al. [2012], and it requires thousands of physical qubits for a logical qubit with the current performance of the physical qubits. This is very challenging to realize since the qubits have to be operating in a dilution refrigerator at very low temperature of only 20mK. If we want to build a quantum computer with 5000 logical qubits, we will need to build quantum chips

with millions of physical qubits, and be able to control each individual one of them, all under 20mK. There are many engineering efforts targeting this challenge and eventually it could be made possible, and naturally another way of solving this problem is to improve the performance of physical qubits and reduce the number of qubits needed for a logical qubit.

Currently, most of the superconducting quantum computers are constructed with transmon qubits. It was first designed and built in Yale, and has very good properties for quantum computation. Transmons have very simple structures, which makes it easy to fabricate in a large amount. Despite being sensitive to charge drive, its coherences T_1 and T_2 are both good and still have room for improvement. However, as a weak anharmonic system, the transmon qubit has a $|e\rangle \rightarrow |f\rangle$ transition frequency close to its qubit frequency, and this puts a limit on the gate speed for the transmon qubits. A typical transmon qubit has qubit frequency around 5GHz, anharmonicity $\sim$ 250MHz, and single and two qubit gate around 20ns. For a nonideal oscillator, its radiation loss rate is usually proportional to the oscillation frequency, thus the loss can be reduced by lowering its frequency. With this motivation, we explore another superconducting qubit with much less frequency, and found that it can indeed have longer coherence times, while the single and two qubit gates can be as fast as transmon ones.

This new superconducting qubit design is called fluxonium, which was first discovered at Yale in 2009 Manucharyan et al. [2009]. It was soon discovered that by adding shunting capacitors to the circuit, we can greatly improve its coherence with lower qubit frequency. It immediately raised the question of how to operate the qubit quickly when its frequency is much lower than majority of the superconducting qubits, and we would like to answer this question with the works in this thesis.

The first problem to solve is the qubit thermal population. According to Boltzmann distribution, a very low frequency excited level will be significantly populated even at fridge temperature of 20mK, thus we will need ways to initialize the qubit before any logical operations. We subsequently demonstrate ultra-fast single qubit gate protocols that can

perform arbitrary single qubit rotations with speed on par with the transmon ones. We also present a tunable coupler design that works with low-frequency fluxoniums, and two qubit $\sqrt{b\text{SWAP}}$ gates within 100ns with 99.91% gate fidelity.

The structure of this thesis is as follows: in chapter two, we introduce circuit QED with fluxonium qubits as its components. Chapter three discusses the on-chip design and fabrications of the devices, and the measurement and analysis of their physical properties like coherence. Chapter four describes the laboratory setup for the experiments we performed, including fridge wiring and room temperature instruments. Chapter five presents the qubit initialization and readout protocols specifically necessary for low frequency qubits. Chapter six demonstrates the fast, high-fidelity single qubit gates with Landau-Zener transition. Finally, chapter eight demonstrates the tunable coupler design for realizing fast two qubit gates for fluxonium qubits. With protocols for qubit initialization, single and two qubit gates, and qubit readout developed, we believe that the fluxonium qubits are ready for scaling up.

CHAPTER 2

CIRCUIT QED WITH FLUXONIUM QUBITS

To describe the quantum properties of superconducting circuits, we start with circuit quantum electrodynamics (circuit QED).

2.1 Circuit Quantization

It was shown that a linear reciprocal lossless multiport circuit can be represented by either a canonical Foster impedance model or a canonical Foster admittance model (Cauer and Belevitch) Russer and Russer [2012]. This is also true for distributed linear reciprocal lossless electromagnetic structures according to Russer et al. (2002), Russer (2006), and Felsen et al. (2009). The canonical Foster admittance multiport representation is a parallel connection of elementary multiports, each of which consists of a series resonant circuit or an inductor and ideal transformers. The canonical Foster impedance multiport representation is a series connection of elementary multiports, each of which consists of a parallel resonant circuit or a capacitor and ideal transformers. The two circuits are dual to each other, and their Lagrangians are

$$L_{admittance} = \sum_{v=1}^{N} (\frac{L_v}{2} \dot{q}_v^2 - \frac{1}{2C_v} q_v^2) \tag{2.1}$$

$$L_{impedance} = \sum_{v=1}^{N} (\frac{C_v}{2} \dot{\phi}_v^2 - \frac{1}{2L_v} \phi_v^2) \tag{2.2}$$

respectively. The charges q_v and magnetic fluxes ϕ_v are state variables for the two representations, and they are related in the following way

$$\phi_v = \frac{\partial L}{\partial \dot{q}_v} = L_v \dot{q}_v \tag{2.3}$$

$$q_v = \frac{\partial L}{\partial \dot{\phi}_v} = C_v \dot{\phi}_v \tag{2.4}$$

Since $\dot{q}_v$ is the current through the inductor L_v, and $\dot{\phi}_v$ is the voltage across the capacitor C_v, with both representations we can derive the same hamiltonian

$$H = \sum_{v=1}^{N} (\frac{1}{2L_v}\phi_v^2 + \frac{1}{2C_v}q_v^2) \tag{2.5}$$

and its equation of motion

$$\frac{df}{dt} = \{f, H\} + \frac{\partial f}{\partial t} \tag{2.6}$$

where $\{f, H\}$ is the Poisson bracket of f and H.

A typical example of electric circuit is an LC resonator, which consists of an inductor L and a capacitor C. The total energy of this oscillator is given by its Hamiltonian $H_{LC} = \frac{q^2}{2C} + \frac{\phi^2}{2L}$, where q is the charge across the capacitor and ϕ is the flux through the inductor. Another circuit element widely used in superconducting circuits is a Josephson junction. It consists of two superconductors weakly coupled across a tunnel barrier. In the regime where the voltage across the junction is much less than the energy gap, the current through the junction is related to the quantum phase difference with

$$I(t) = I_c \sin \phi(t) \tag{2.7}$$

where I_c is the critical current of the Josephson junction.

For quantization of a classical circuit, the charge and flux variables are promoted to non-commuting observables with the commutation relation

$$[\hat{\phi}_u, \hat{q}_v] = \hat{\phi}_u \hat{q}_v - \hat{q}_v \hat{\phi}_u = i\hbar\delta_{uv} \tag{2.8}$$

with time evolution of operator $f(t)$ as

$$i\hbar \frac{df(t)}{dt} = [f(t), H] + \frac{\partial f(t)}{\partial t}. \tag{2.9}$$

It is useful to introduce the standard creation and annihilation operators ($\hat{a}_v^\dagger$ and $\hat{a}_v$) so that

$$\hat{\phi}_v = \phi_{zpf}(\hat{a}_v^\dagger + \hat{a}_v), \qquad \hat{q}_v = iq_{zpf}(\hat{a}_v^\dagger - \hat{a}_v) \tag{2.10}$$

where $\phi_{zpf} = \sqrt{\hbar/2\omega_v C} = \sqrt{\hbar Z_v/2}$ and $q_{zpf} = \sqrt{\hbar\omega_v C/2} = \sqrt{\hbar/2Z_v}$ are the characteristic magnitude of the zero-point fluctuations of the flux and the charge. With these definitions, we can write the quantum Hamiltonian of the quantized circuit as

$$H = \frac{1}{2}\sum_{v=1}^{N} \hbar\omega_v (a_v^\dagger a_v + a_v a_v^\dagger). \tag{2.11}$$

For example, the Hamiltonian of an LC resonator is $\hat{H}_{LC} = \hbar\omega_r(\hat{a}^\dagger\hat{a} + 1/2)$, and the Hamiltonian of a Josephson junction is $\frac{I_c\Phi_0}{2\pi}\cos\hat{\phi}$.

2.2 Fluxonium qubit coupled to an LC resonator

The fluxonium circuit consists of a small-area Josephson junction (JJ) with inductance L_J shunted by a large inductance (L_{JA}), and a large capacitor (C_q), as shown in Fig. 2.1. The

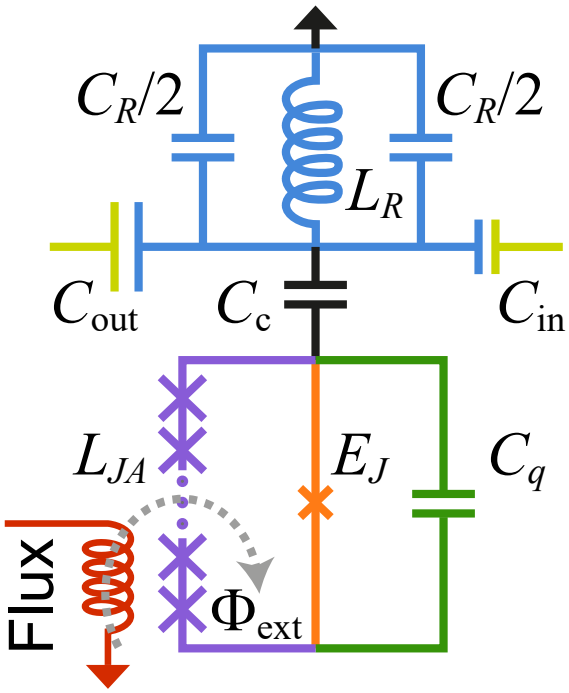

Figure 2.1: **Circuit diagram for the heavy-fluxonium qubit**

Hamiltonian of a fluxonium qubit is

$$H_f = -4E_C \frac{d^2}{d\varphi^2} - E_J \cos\left(\varphi - 2\pi\frac{\Phi_{\text{ext}}}{\Phi_0}\right) + \frac{1}{2}E_L\varphi^2, \tag{2.12}$$

where $E_C = e^2/(2C_q)$ is the charging energy, $E_J = \Phi_0^2/(4\pi^2 L_J)$ the Josephson energy of the small junction, and $E_L = \Phi_0^2/(4\pi^2 L_{JA})$ the inductive energy of the JJ array. Φ_{ext} denotes the flux threading the loop formed by the small junction and the super-inductance, and Φ_0 is the quantum of flux.

The fluxonium qubit is a very nonlinear quantum system, and we usually calculate the eigenenergies and eigenstates by diagonalizing the Hamiltonian numerically instead of working with approximations from perturbation theory. The potential energy and level structure of a fluxonium at the flux-frustration point ($\Phi_{\text{ext}} = \Phi_0/2$) is shown in Fig. 2.2. There are two types of transitions of interest, the intra-well plasmons ($|g\rangle \leftrightarrow |h\rangle$ and $|e\rangle \leftrightarrow |f\rangle$) and

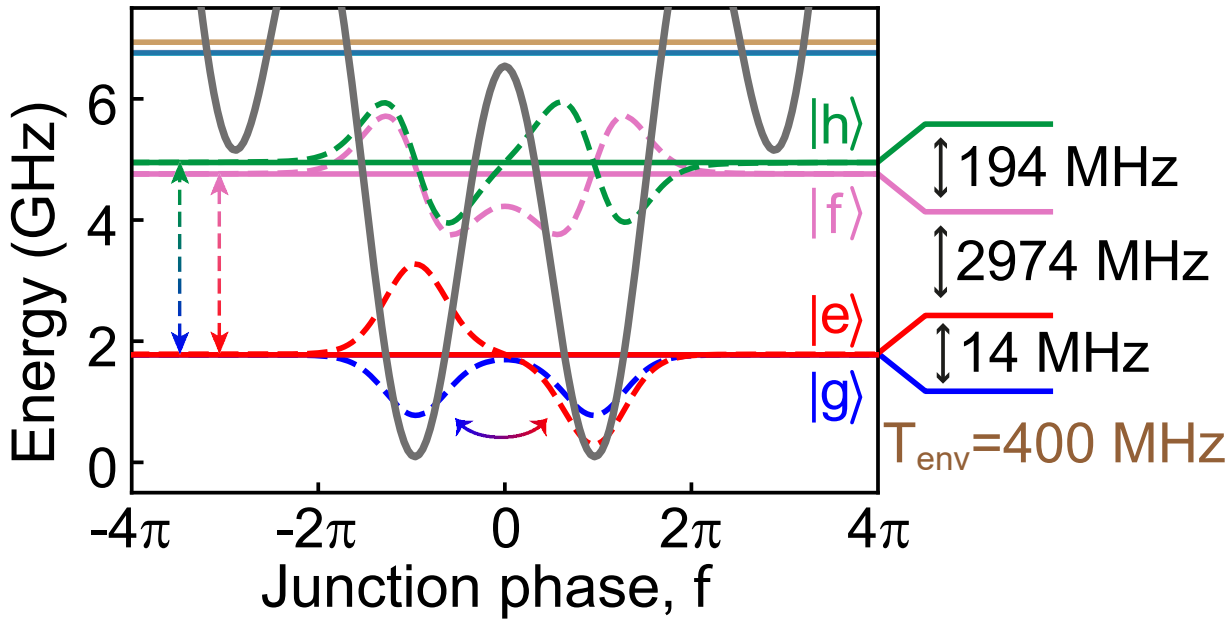

Figure 2.2: **Energy-level diagram of the heavy-fluxonium at the flux-frustration point ($\Phi_{\text{ext}} = \Phi_0/2$).** The gray line represents the potential well. The first six energy eigenstates are depicted by the colored lines; dashed lines show the wavefunctions for the first four levels with corresponding color. The fluxon-like transition $|g\rangle \leftrightarrow |e\rangle$ is marked with a solid arrow, while plasmon-like transitions $|g\rangle \leftrightarrow |h\rangle$ and $|e\rangle \leftrightarrow |f\rangle$ are marked with dashed arrows.

inter-well fluxons ($|g\rangle \leftrightarrow |e\rangle$ and $|f\rangle \leftrightarrow |h\rangle$). Since the wavefunctions of $|g\rangle$ and $|f\rangle$ are both even in phase space, and $|e\rangle$ and $|h\rangle$ are both odd, the single-photon transitions $|g\rangle \leftrightarrow |f\rangle$ and $|e\rangle \leftrightarrow |h\rangle$ are forbidden at the flux-frustration point due to the parity selection rule. The qubit is comprised of the lowest two energy levels $|g\rangle, |e\rangle$, with the qubit transition being fluxon like, with a very low frequency typically between 15MHz to 2GHz.

The fluxonium qubit is usually capacitively coupled to an LC resonator for readout purposes. The total system Lagrangian is

$$L = T_f + T_r + V_f + V_r + \frac{C_c}{2}(\dot{\phi}_f - \dot{\phi}_r)^2 \tag{2.13}$$

where T_f and T_r are kinetic terms for the fluxonium and resonator, and V_f and V_r are potential terms for the fluxonium and resonator. We can thus derive the system Hamiltonian

H with the circuit quantization procedure described in the previous chapter

$$H = H'_r + H'_f + g n_r n_f \tag{2.14}$$

where

$$H'_r = \frac{n_r^2}{2(C_r + C_c)} + \frac{L_r \phi_r^2}{2} \tag{2.15}$$

$$H'_f = \frac{n_f^2}{2(C_f + C_c)} + E_J \cos\phi_f + \frac{E_L}{2}\phi_f^2 \tag{2.16}$$

and $g = \frac{C_c}{(C_f+C_c)(C_r+C_c)}$. By diagonalizing the full Hamiltonian, we can derive the eigenlevels for the dressed states mixed by qubit and resonator bare eigenstates. We usually work in the dispersive regime where the coupling g is small, and the dressed eigenstates can still be labeled with qubit and resonator levels.

To calculate the dispersive shift χ of resonator frequencies, we calculate $f_{e1} - f_{e0} - f_{g1} + f_{g0}$, where g and e label the qubit ground and excited states, and 0 and 1 label the number of photons in the LC resonator. We can see that the qubit population shifts the resonator frequency by 2χ, and same for resonator population shift on the qubit frequency.

CHAPTER 3

DEVICE DESIGN AND FABRICATION

3.1 Fluxonium qubits on a 2D chip

We realized the fluxonium system discussed previously on a 2D chip with standard circuit QED components (capacitors, Josephson junctions and planar structures). The shunting inductance is realized by an array of 300 large-area JJs each having a Josephson energy E_{JA} and charging energy E_{CA}. We make $E_{JA}/E_{CA} \gg 1$ to ensure that the charge dispersion for each array junctions is small, and the array can be regarded as a linear inductor. The corresponding chip image is shown in Fig. 3.1, and effective circuit is shown in Fig. 2.1, resulting in the Hamiltonian we wanted

$$H_f = -4E_C\frac{d^2}{d\varphi^2} - E_J\cos\left(\varphi - 2\pi\frac{\Phi_{\text{ext}}}{\Phi_0}\right) + \frac{1}{2}E_L\varphi^2, \tag{3.1}$$

The corresponding values for our single qubit device are: $E_C/h = 0.479$ GHz, $E_L/h = 0.132$ GHz, and $E_J/h = 3.395$ GHz where h is Planck's constant.

We increased the qubit frequencies for the two fluxonium qubits, with qubit parameters $E_C1/h = 0.952$ GHz, $E_{L1}/h = 0.269$ GHz, $E_{J1}/h = 5.645$ GHz, and $E_{C2}/h = 0.898$ GHz, $E_{L2}/h = 0.268$ GHz, $E_{J2}/h = 4.855$ GHz, where h is Planck's constant (see table 3.1). The level structure of the two fluxonium qubits at the flux-frustration point ($\Phi_{\text{ext}} = \Phi_0/2$) is shown in Fig. 3.4. Due to the high E_J/E_C ratio for both qubits, we have low qubit frequencies ($\omega_{ge1} = 48$MHz, $\omega_{ge2} = 61MHz$), and large anharmonicity $\alpha_1 = 5$GHz, $\alpha_2 = 5$GHz (see table 3.2). We have a gmon style tunable coupler between the two fluxonium qubits (shown in Fig. 3.2), and the effective circuit is shown in Fig. 3.3.

Spectroscopies of higher energy plasmon levels are used to determine the system parameters. We can observe the plasmon transitions with pulse probe experiment, where the qubits are charge driven through the readout resonator. We subsequently fitted the spectroscopy

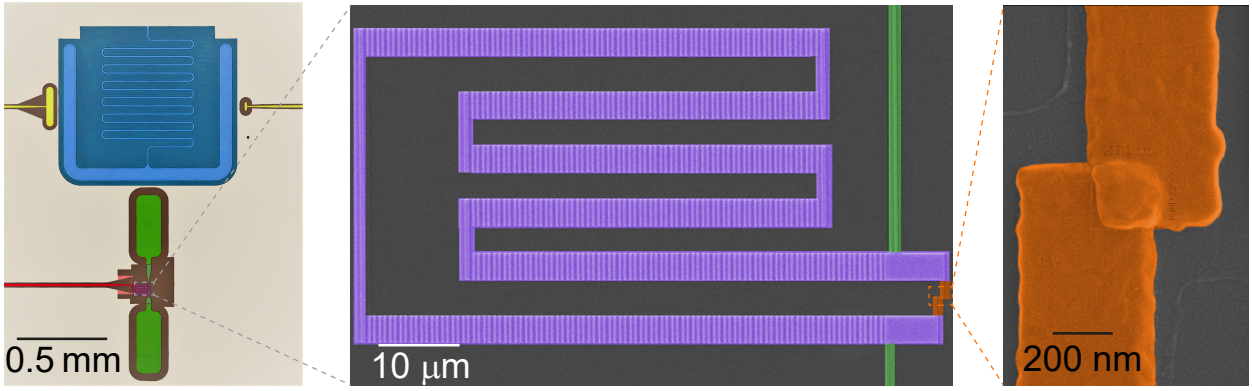

Figure 3.1: **Device image.** Left panel: False-colored optical microscope image of the fluxonium coupled to a readout resonator (blue) along with flux (red) and input-output (yellow) lines. Middle panel: scanning electron micrograph of the large junction array (purple), and the small Josephson junction (orange). Right panel: zoom-in view of the small junction.

Table 3.1: **Circuit parameters in h·GHz used in two qubit experiment.**

	E_J	E_C	E_L	E_{C+}	E_{C-}
qubit a	5.65	0.95	0.292		
qubit b	4.88	0.905	0.286		
coupler	4.246		3.52	12.0	8.0

data with full numeric model, and the fitting is shown in fig 3.5.

3.2 Device Fabrication

The single qubit device (shown in Fig. 3.1 in the previous section) was fabricated on a 430 μm thick C-plane sapphire substrate. The base layer of the device, which includes the majority of the circuit (excluding the Josephson junctions), consists of 150 nm of niobium deposited via electron-beam evaporation, with features fabricated via optical lithography and reactive ion etch (RIE) at wafer-scale. 600 nm thick layer of AZ MiR 703 was used as the (positive) photoresist, and the large features were written using a Heidelberg MLA 150 Direct Writer, followed by RIE performed using a PlasmaTherm ICP Fluorine Etch tool. The junction mask was fabricated via electron-beam lithography with a bi-layer resist (MMA-PMMA) comprising of MMA EL11 and 950PMMA A7. The e-beam lithography was performed on a

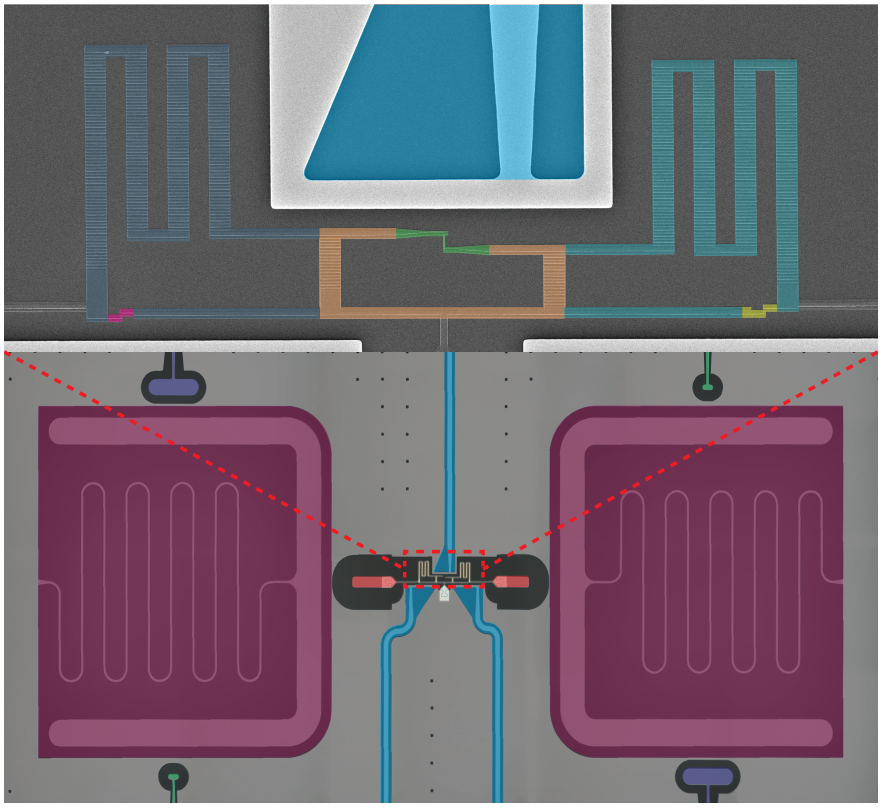

Figure 3.2: **Device image of two fluxonia with a tunable coupler.** Top panel: False-colored scanning electron microscope image of the two fluxoniums and coupler junction loops. Bottom panel: optical microscope image of the flux control lines, readout resonators, qubit shunting capacitors, and resonator drive and readout lines.

Raith EBPG5000 Plus E-Beam Writer. All Josephson junctions were made with the Dolan bridge technique. They were subsequently evaporated in Plassys electron beam Evaporator with double angle evaporation ($\pm 19^o$). The wafer was then diced into 7×7 mm chips, mounted on a printed circuit board, and subsequently wire-bonded.

The two qubit device (shown in Fig. 3.2 in the previous section) was fabricated on a 430 μm thick C-plane sapphire substrate. The base layer of the device, which includes the majority of the circuit (excluding the Josephson junctions), consists of 200 nm of tantalum with features fabricated via optical lithography and HF etch at wafer-scale. We perform standard TAMI cleanning for annealed sapphire substrates, followed with nanostrip etching at 50C for 10 minutes, and sulfuric acid etching at 140C for 10 minutes. We subsequently

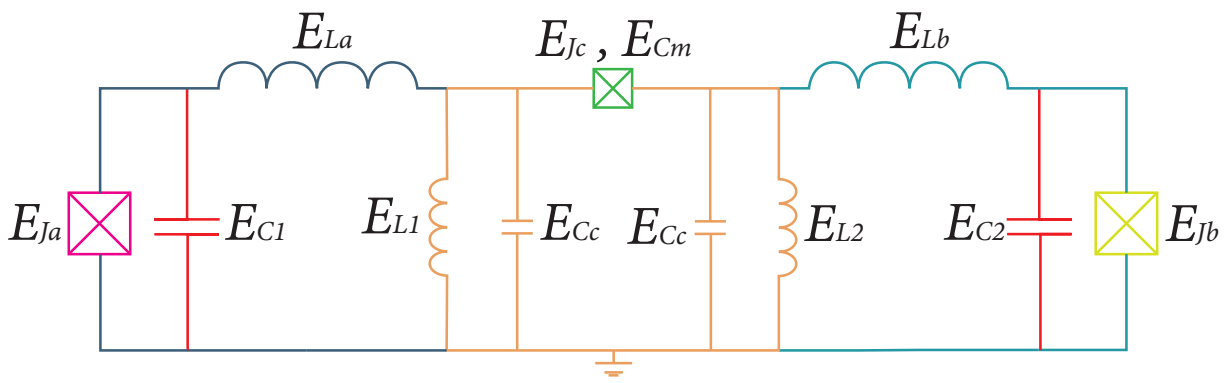

Figure 3.3: **Circuit diagram for the coupled fluxoniums with the tunable coupler**

Table 3.2: **Energy splittings and anharmonicities of the bare modes, and coherences for the qubits.** The fluxonium qubits are biased at their half-flux sweet spots while the coupler θ_- mode is biased at $\Phi_c/\Phi_0 = 0.3$. The energy splittings are differences between the bare ground and first-excited state energies $E_{10} = E_1 - E_0$, while the anharmonicity is defined as $\alpha = E_{21} - E_{10}$.

	qubit a	qubit b	coupler θ_-	coupler θ_+
E_{10} (GHz)	0.0618	0.0484	11	30
α (GHz)	4.3	4.9	0.53	0
T_1 (μs)	180	300		
T_{2e} (μs)	250	300		

deposit 200nm tantalum in AJA ATC 2200 sputtering tool at 800C. Then 2000 nm thick layer of AZ 1518 was used as the (positive) photoresist, and the large features were written using a Heidelberg MLA 150 Direct Writer, followed by HF etching performed with Ta etchant 1:1:1. The junction mask was fabricated via electron-beam lithography with a bi-layer resist (MMA-PMMA) comprising of MMA EL11 and 495PMMA A6. The e-beam lithography was performed on a Raith EBPG5000 Plus E-Beam Writer. All Josephson junctions were made with the Dolan bridge technique. They were subsequently evaporated in Plassys electron beam Evaporator with double angle evaporation ($\pm 21^o$). The wafer was then diced into 7×7 mm chips, mounted on a printed circuit board, and subsequently wire-bonded.

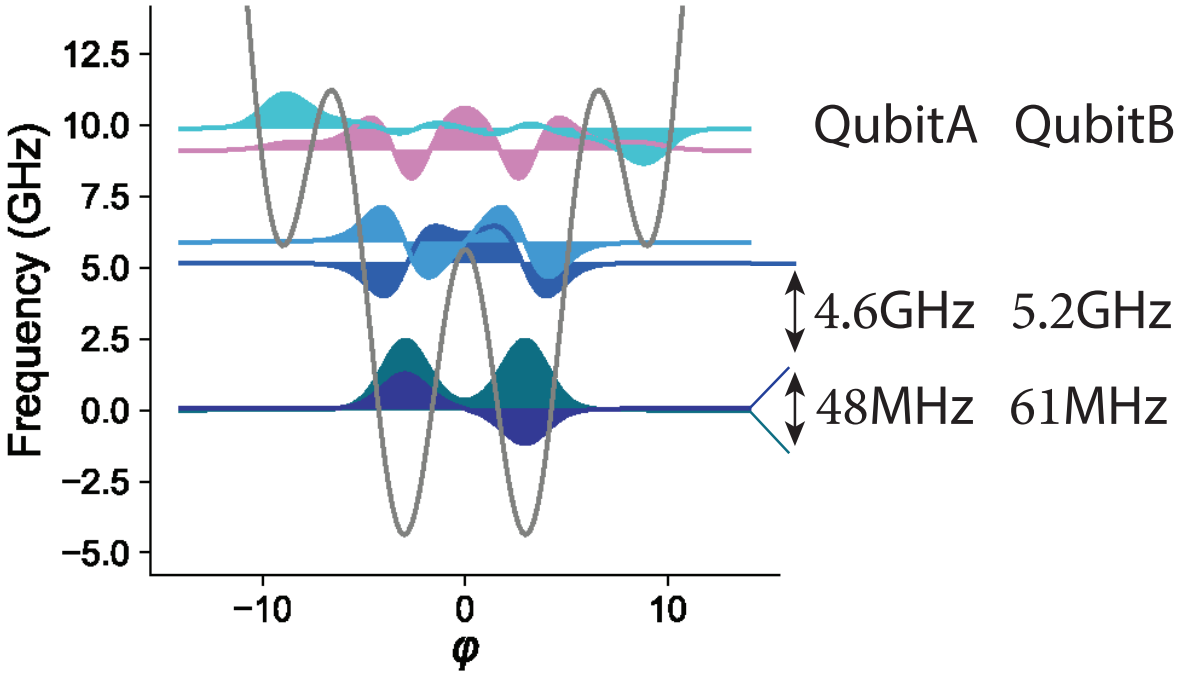

Figure 3.4: **Energy-level diagram of the heavy-fluxonium at the flux-frustration point ($\Phi_{\text{ext}} = \Phi_0/2$).** The gray line represents the potential well. The first six energy eigenstates and wavefunctions are plotted with the colored lines. The qubit frequencies, anharmonicities, and resonator detunings for each qubit are marked with black arrows.

3.3 Qubit relaxation measurement and analysis

We measured and systematically calculated the qubit coherence in the single and two qubit fluxonium devices. Fig. 3.6 shows the experimentally measured T_1 (black circles) as a function of applied external flux while the inset shows a $T_1 = 315 \pm 10$ μs measured at the flux-frustration point ($\star$) following initialization of the qubit in either the $|g\rangle$ or $|e\rangle$ state. The qubit relaxes to a near equal mixture where the excited state population $P(|e\rangle) = 0.4955 \pm 0.0015$, with the deviation providing an estimate of the temperature of the surrounding bath, $T = 42 \pm 14$ mK. At the flux-frustration point, the wavefunctions are delocalized into symmetric and anti-symmetric combinations of the states in each well. As we move away from this degeneracy point, the wavefunctions localize into different wells resulting in a suppression of tunneling and an increase in the relaxation times, see Fig. 3.6.

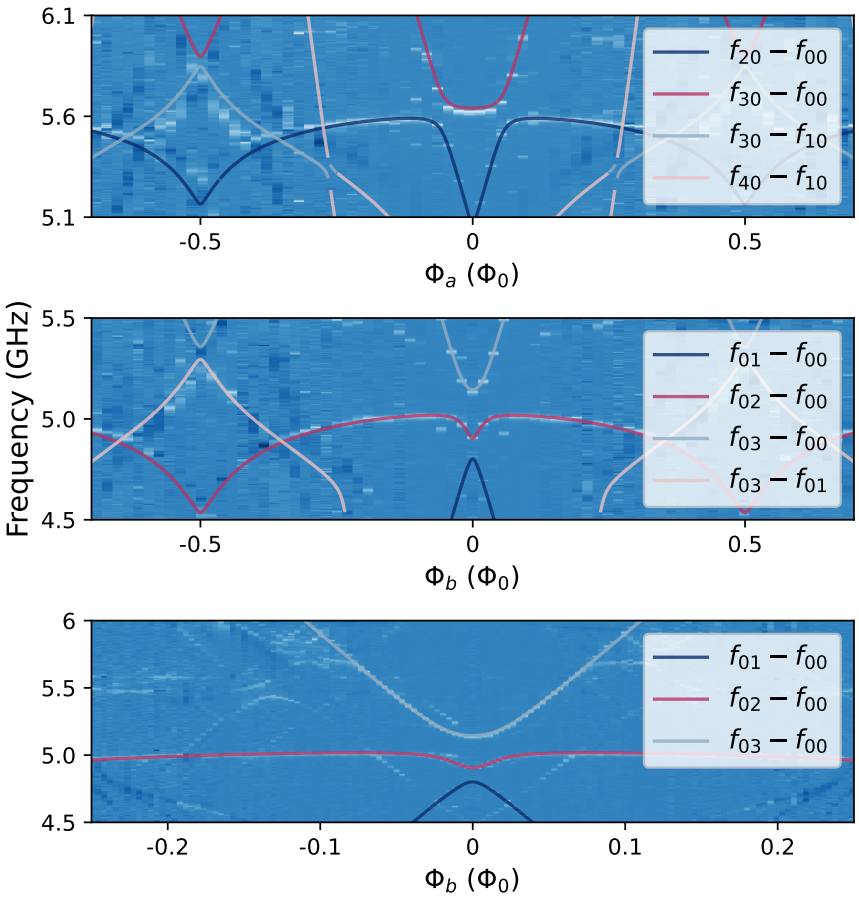

Figure 3.5: **Plasmon spectroscopy features of both qubits.** Top panel: $|00\rangle \rightarrow |20\rangle$ and $|00\rangle \rightarrow |30\rangle$ transition frequency vs qubit A flux bias. Middle panel: $|00\rangle \rightarrow |02\rangle$ and $|00\rangle \rightarrow |03\rangle$ transition frequency vs qubit B flux bias. Bottom panel: zoomed in plot around $\Phi_B = 0$. The data was taken with coupler flux around 0, and the other qubit's flux fixed at 0.

Here, the qubit relaxation times are measured over a wide range of external flux by driving the $|g\rangle - |h\rangle$ transition for 120 μs (five times of the $|h\rangle$ state T_1) to ensure most of the population reside in the $|e\rangle$ state, and monitoring the subsequent decay. While moving away from the flux-frustration point, T_1 increases to a maximum value of 4.3 ± 0.2 ms, consistent with previous heavy-fluxonium devices Earnest et al. [2018], Nguyen et al. [2019], before subsequently decreasing.

To explain the measured relaxation times, we consider several avenues by which the qubit can decay, including Purcell loss, decay via charge and flux coupling to the control

lines, $1/f$ flux noise, dielectric loss in the capacitor, and resistive loss in the superinductor. Conservative estimates of the flux noise induced loss are lower than the measured loss by nearly an order of magnitude. The loss near the flux-frustration point is believed to be largely due to dielectric loss in the capacitor. This can be thought of as Johnson-Nyquist current noise from the resistive part of the shunting capacitor, which couples to the phase matrix element $\langle g|\hat{\varphi}|e\rangle$, and grows rapidly as we approach the flux-frustration point Nguyen et al. [2019]. Assuming a fixed loss tangent for the capacitor, this loss rate is inversely proportional to the impedance of the capacitor, and is given by:

$$\Gamma_{\text{diel}} = \frac{\hbar\omega_q^2}{4E_C Q_{\text{cap}}} \coth\left(\frac{\hbar\omega_q}{2k_B T}\right) |\langle g|\hat{\phi}|e\rangle|^2. \tag{3.2}$$

The T_1 at the flux-frustration point sets an upper bound of $1/Q_{\text{cap}} = 4 \times 10^{-6}$ for the loss tangent of the capacitor, which is within a factor of two of the value reported in previous heavy-fluxonium devices Nguyen et al. [2019], and results in the dashed red curve in Fig. 3.6. Since ω_q is below the ambient temperature near the flux-frustration point, a combination of the temperature-dependent prefactor $\sim 2k_B T/(\hbar\omega_q)$, and the relation between charge and phase matrix elements in fluxonium, $\langle g|\hat{n}|e\rangle = \omega_q/(8E_c)\langle g|\hat{\phi}|e\rangle$, results in the dielectric-loss scaling as $1/\omega_q$, which is consistent with the observed trend in the T_1 near the flux-frustration point. The measured T_1 at the flux-frustration point also sets an upper bound of 1.7×10^{-9} for the loss tangent of the inductor. The decay from inductive loss, however, increases more rapidly with frequency than dielectric loss ($\propto 1/\omega_q^3$) and is inconsistent with measured data. Our qubit operations are performed between $0.4\Phi_0 - 0.5\Phi_0$ where the T_1 is mainly limited by dielectric loss. As we move further away from the flux-frustration point ($\sim 0.4\Phi_0$), T_1 starts to decrease. This additional loss is believed to be due to a combination of radiative loss to the charge drive line, and Purcell loss from higher fluxonium levels excited by heating from the $|g\rangle$ and $|e\rangle$ states. The Purcell loss calculated based on the coupled fluxonium-resonator system using a bath temperature of 60 mK results in the dotted blue curve shown in Fig. 3.6.

This is slightly higher than the temperature inferred from the qubit thermal steady state population, and can be attributed to the fact that the noise environments could be significantly different at frequencies that are more than two orders of magnitude apart. The enhanced loss near $\Phi_{\text{ext}} = 0.35\Phi_0$ is suggestive that heating to higher levels may contribute as there are several near resonances of higher fluxonium levels with the readout resonator, which depend sensitively on the circuit parameters.

To explain the measured relaxation times of the fluxonium, we consider decay via charge and flux coupling to the control lines, $1/f$ flux noise, dielectric loss in the capacitor, resistive loss in the superinductor, and Purcell loss. The decay rates arising from these loss mechanisms are derived using Fermi's golden rule, with the bath described using the Caldeira-Leggett model Schoelkopf et al. [2003], Clerk et al. [2010]. For a noise source with amplitude $f(t)$ and coupling constant α between the fluxonium qubit states, the interaction Hamiltonian can be written as $H' = \alpha f(t)\sigma_x$ in the qubit subspace. This results in a qubit depolarization rate,

$$\Gamma = \frac{\alpha^2}{\hbar^2}(S_f(+\omega_{01}) + S_f(-\omega_{01})). \tag{3.3}$$

Here $S_f(\omega) = \int_{-\infty}^{\infty} e^{i\omega\tau} \langle f(\tau)f(0)\rangle$ is the noise spectral density associated with the source. We note that at a finite bath temperature corresponding to an inverse temperature $\beta = \frac{1}{k_B T}$, detailed balance relates the positive and negative frequency components of the noise spectral density as $S_f(-\omega)/S_f(\omega) = e^{-\beta\hbar\omega}$. Depending on the noise source f, the coupling constant α is proportional to the charge or phase matrix element of the fluxonium. Since the only term in the Hamiltonian that does not commute with $\hat{\phi}$ is the charging energy $4E_c\hat{n}^2$, and $[\hat{\phi}, \hat{n}] = i$,

$$\begin{aligned} \langle j| [\hat{\phi}, \hat{H}] |k\rangle &= (\omega_j - \omega_k) \langle j| \hat{\phi} |k\rangle \\ &= i(8E_c) \langle j| \hat{n} |k\rangle . \end{aligned} \tag{3.4}$$

The matrix elements of the fluxonium circuit are thus related by $|\langle g0|\hat{n}|g1\rangle| = (\frac{\omega}{8E_c})|\langle g0|\hat{\phi}|g1\rangle|$ for all flux values.

3.3.1 Relaxation from flux noise

Flux noise couples to the phase degree of freedom with an interaction strength that depends on the inductive energy E_L. Expanding the fluxonium potential to lowest order in flux results in a coupling constant of $\alpha = 2\pi E_L \langle g0|\hat{\varphi}|g1\rangle/\Phi_0$. We consider flux noise contributions from current noise in the flux-bias line, as well as $1/f$ flux noise. In our experimental setup, the current noise is believed to be mainly due to resistive Johnson-Nyquist noise arising from a 10 dB attenuator with resistance $R = 26\ \Omega$ (last resistor in T network) on the fast flux line, corresponding to current noise spectral density of $S_I(\omega) = \frac{2}{R}\frac{\hbar\omega}{\left(1-e^{-\beta\hbar\omega}\right)}$, with the expected interpolation between quantum and thermal noise. This is related to flux noise by the mutual inductance $M = \Phi_0/1.6$ mA between flux line and the qubit, obtained from the DC flux period. Therefore, $S_f(\omega) + S_f(-\omega) = 2\hbar\omega\frac{M^2}{R}\coth\left(\frac{\beta\hbar\omega}{2}\right)$, and the decay rate

$$\Gamma_R = \pi^3 \left(\frac{R_Q}{R}\right)\left(\frac{M}{L}\right)^2 |\langle g0|\hat{\varphi}|g1\rangle|^2 \omega \coth\left(\frac{\beta\hbar\omega}{2}\right), \tag{3.5}$$

where $R_Q = h/e^2$ is the resistance quantum, and L is the fluxonium inductance.

For $1/f$ flux noise, the noise spectral density is of the form $S_\Phi(\omega) = 2\pi\eta^2/\omega$, with the resulting decay rate,

$$\Gamma_{1/f} = 8\pi^3 \left(\frac{E_L}{\hbar}\right)^2 \left(\frac{\eta}{\Phi_0}\right)^2 \frac{|\langle g0|\hat{\varphi}|g1\rangle|^2}{\omega}. \tag{3.6}$$

The $1/f$ noise amplitude is fit from T_{2e} data, and corresponds to $\eta = 5.21\ \mu\Phi_0$. The suppression of the $1/f$ noise induced decay by E_L^2, results in a limit of $T_1 = 2.4$ ms for the relaxation time at the flux-frustration point, which grows rapidly ($\propto \omega^3$) as we move away from it.

3.3.2 Relaxation from radiative loss to the charge line

In addition to current noise, the fluxonium could also be affected by radiative loss arising from Johnson-Nyquist voltage noise ($S_V(\omega) = \frac{2R\hbar\omega}{1-e^{-\beta\hbar\omega}}$) that couples to the qubit via spurious charge coupling, with the resistance R serving as a phenomenological parameter. In this case, the coupling constant is related to the charge matrix element as $\alpha = 2e\langle g0|\hat{n}|g1\rangle$, and $S_f(\omega) + S_f(-\omega) = 2R\hbar\omega \coth\left(\frac{\beta\hbar\omega}{2}\right)$. The resulting decay rate is,

$$\Gamma_c = \frac{\omega}{Q_c}\coth\left(\frac{\beta\hbar\omega}{2}\right)|\langle g0|\hat{n}|g1\rangle|^2, \tag{3.7}$$

where $Q_c = \frac{R_Q}{16\pi R}$. An upper-bound for the resistance R can be found using the plasmon T_1 of 10 μs, corresponding to a total quality factor of 1.86×10^5, and $Q_c = 7.4 \times 10^4$. This results in a fluxon T_1 limit in excess of 60 ms at the flux-frustration point.

3.3.3 Relaxation from dielectric loss in the capacitor

Dielectric loss associated with the capacitor can be thought of as Johnson-Nyquist current noise from the resistive part of the shunting capacitor, which couples to the phase matrix element $\langle g|\hat{\varphi}|e\rangle$. This loss rate is therefore inversely proportional to the impedance of the capacitor, assuming a fixed loss tangent ($1/Q_{\text{diel}}$) for the capacitor. As a result, $S_f(\omega) + S_f(-\omega) = \frac{2\hbar\omega^2 C}{Q_{\text{diel}}}\coth\left(\frac{\beta\hbar\omega}{2}\right)$, and

$$\Gamma_{\text{diel}} = \frac{\hbar\omega^2}{4E_C Q_{\text{cap}}}\coth\left(\frac{\beta\hbar\omega}{2}\right)|\langle g0|\hat{\phi}|g1\rangle|^2. \tag{3.8}$$

If the T_1 at the frustration point were limited by dielectric loss, a bath temperature of 42 mK would result in $Q_{\text{cap}} = 1/(4 \times 10^{-6})$. This loss tangent is slightly larger, but within a factor of three of that observed in similar fluxonium devices Nguyen et al. [2019]. Dielectric loss is believed to be the dominant loss channel near the frustration point, also capturing the flux

and frequency dependence of the measured loss ($\propto 1/\omega$).

3.3.4 Relaxation from resistive loss in the inductor

For inductive loss, we again assume a frequency independent loss tangent ($L \rightarrow L(1 + i/Q_{\text{ind}})$), resulting in Johnson-Nyquist current noise that is inversely proportional to the impedance of the superinductor, i.e., $S_f(\omega) + S_f(-\omega) = \frac{\hbar}{LQ_{\text{ind}}} \coth\left(\frac{\beta\hbar\omega}{2}\right)$. The inductive loss is thus,

$$\Gamma_{\text{ind}} = \frac{2E_L}{\hbar Q_L} \coth\left(\frac{\beta\hbar\omega}{2}\right) |\langle g0|\hat{\phi}|g1\rangle|^2. \tag{3.9}$$

The superinductor is extremely low loss, with a quality factor of $Q_{\text{ind}} = 8 \times 10^9$ resulting in a limit of $T_1 = 4$ ms at the flux-frustration point, growing as ω^3 as we move away from the flux-frustration point.

3.3.5 Relaxation rate due to the Purcell Effect

We derive the Purcell relaxation rates of the fluxonium levels, arising from coupling to the resonator by closely following Ref. Groszkowski et al. [2018]. We model this by assuming that the resonator is coupled to a bath of harmonic oscillators, whose Hamiltonian reads

$$H_{\text{bath}} = \sum_k \hbar\omega_k b_k^\dagger b_k, \tag{3.10}$$

where b_k is the lowering operator for mode k. The interaction Hamiltonian between the bath and the resonator is given by

$$H_{\text{int}} = \hbar \sum_k \lambda_k (a b_k^\dagger + a^\dagger b_k), \tag{3.11}$$

where a is the lowering operator for the resonator. Finally, the system under consideration is the fluxonium circuit coupled to the resonator, which we write in the dressed basis as

$$H_{\text{flux+res}} = \sum_k E_k^{\text{flux+res}} \left|\psi_k^{\text{flux+res}}\right\rangle \left\langle\psi_k^{\text{flux+res}}\right|. \tag{3.12}$$

We treat H_{int} as a perturbation which can induce transitions among the eigenstates of the Hamiltonian $H = H_{\text{bath}} + H_{\text{flux+res}}$, given by

$$|\psi_i\rangle = \left|\psi_i^{\text{flux+res}}\right\rangle \bigotimes_k |m_k\rangle\,. \tag{3.13}$$

The transition rate under the action of a constant perturbation is given by Fermi's Golden Rule in the form

$$\gamma_{i\to f} = \frac{2\pi}{\hbar}\delta(E_i - E_f)|\left\langle\psi_f\right|H_{\text{int}}\left|\psi_i\right\rangle|^2, \tag{3.14}$$

where E_i and E_f are the eigenenergies of the states $|\psi_i\rangle$ and $\left|\psi_f\right\rangle$, respectively. These energies are

$$\begin{aligned} E_i &= E_i^{\text{flux+res}} + \hbar\sum_k m_k\omega_k, \\ E_f &= E_f^{\text{flux+res}} + \hbar\sum_k m'_k\omega_k, \end{aligned} \tag{3.15}$$

where $\{m_k\}$ denotes the initial configuration of the bath and $\{m'_k\}$ the final configuration. Inserting the form of H_{int} into Eq. (3.14) and noting that cross-terms vanish leads to

$$\begin{aligned} \gamma_{i,\{m_k\}\to f,\{m'_k\}} = 2\pi\hbar\delta(E_i - E_f)\sum_k |\lambda_k|^2\Big(\Big|\left\langle\psi_f^{\text{flux+res}}\right|a^\dagger\left|\psi_i^{\text{flux+res}}\right\rangle\Big|^2 m_k\delta_{m'_k,m_k-1} \\ + \Big|\left\langle\psi_f^{\text{flux+res}}\right|a\left|\psi_i^{\text{flux+res}}\right\rangle\Big|^2 (m_k+1)\delta_{m'_k,m_k+1}\Big)\prod_{k'\neq k}\delta_{m'_{k'},m_{k'}}, \end{aligned}$$

To find the total transition rate, we must sum over all such initial and final configurations, taking into account the thermal probability of occupying a given initial configuration:

$$\Gamma_{i\to f} = \sum_{\{m_k\},\{m'_k\}} P(\{m_k\})\gamma_{i,\{m_k\}\to f,\{m'_k\}}, \tag{3.16}$$

where

$$P(\{m_k\}) = \frac{e^{-\sum_k \beta m_k \hbar\omega_k}}{Z}, \tag{3.17}$$

Z is the partition function of the bath and $\beta = 1/k_B T$. Performing the sums over all initial and final states yields

$$\begin{aligned}\Gamma_{i\to f} = 2\pi\hbar \sum_k |\lambda_k|^2 \delta(E_i^{\text{flux+res}} - E_f^{\text{flux+res}} + \hbar\omega_k) \\ \left| \left\langle \psi_f^{\text{flux+res}} \middle| a^\dagger \middle| \psi_i^{\text{flux+res}} \right\rangle \right|^2 n_{\text{th}}(\omega_k) \\ +2\pi\hbar \sum_k |\lambda_k|^2 \delta(E_i^{\text{flux+res}} - E_f^{\text{flux+res}} - \hbar\omega_k) \\ \left| \left\langle \psi_f^{\text{flux+res}} \middle| a \middle| \psi_i^{\text{flux+res}} \right\rangle \right|^2 (n_{\text{th}}(\omega_k) + 1),\end{aligned} \tag{3.18}$$

where

$$n_{\text{th}}(\omega_j) = \sum_{\{m_k\}} P(\{m_k\}) m_j = \frac{1}{e^{\beta\hbar\omega_j} - 1}. \tag{3.19}$$

We next take the continuum limit and define $\kappa = 2\pi\hbar\rho(\omega_k)|\lambda_k|^2$, where $\rho(\omega)$ is the density of states of the bath. Introducing $\omega_{jj'}^{\text{flux+res}} = (E_j^{\text{flux+res}} - E_{j'}^{\text{flux+res}})/\hbar$ leads to the expressions

$$\Gamma_{i\to f}^{\uparrow} = \kappa n_{\text{th}}(\omega_{fi}^{\text{flux+res}}) \left| \left\langle \psi_f^{\text{flux+res}} \middle| a^\dagger \middle| \psi_i^{\text{flux+res}} \right\rangle \right|^2, \tag{3.20}$$

for upward transitions $E_f^{\text{flux+res}} > E_i^{\text{flux+res}}$, and

$$\Gamma_{i\to f}^{\downarrow} = \kappa(n_{\text{th}}(-\omega_{fi}^{\text{flux+res}}) + 1) \left| \left\langle \psi_f^{\text{flux+res}} \middle| a \middle| \psi_i^{\text{flux+res}} \right\rangle \right|^2, \tag{3.21}$$

for downward transitions $E_f^{\text{flux+res}} < E_i^{\text{flux+res}}$. The final step is to note that throughout this experiment, the fluxonium qubit is operated in the dispersive regime with respect to the frequency of the resonator. Therefore, we expect that the dressed eigenstates of $H_{\text{flux+res}}$ can be labeled with quantum numbers ℓ and n, with ℓ labeling the fluxonium state and n the resonator state. When performing numerical simulations, this identification is based on which numbers ℓ and n produce the maximum overlap of the dressed state $\left|\psi_i^{\text{flux+res}}\right\rangle = \left|\overline{\ell, n}\right\rangle$ with the product state $|\ell, n\rangle$. As in Ref. Groszkowski et al. [2018], we are interested mainly in transitions among fluxonium states, where the quantum number ℓ changes. We therefore define the total transition rate due to the Purcell effect among fluxonium states as a sum over all possible initial and final states of the resonator, weighting initial states by their probability of being thermally occupied $P_{\text{res}}(n) = (1 - \exp(-\beta\hbar\omega_r)) \exp(-n\beta\hbar\omega_r)$. This yields

$$\begin{aligned} \Gamma_{\ell\to\ell'}^{\text{Purcell},\uparrow} = \sum_{n,n'} & P_{\text{res}}(n)\kappa n_{\text{th}}(\omega_{\ell',n',\ell,n}) \\ & \times \left| \left\langle \overline{\ell', n'} \middle| a^\dagger \middle| \overline{\ell, n} \right\rangle \right|^2, \end{aligned} \tag{3.22}$$

for upward transitions, where $\omega_{\ell',n',\ell,n} = (E_{\ell',n'} - E_{\ell,n})/\hbar$, and

$$\begin{aligned} \Gamma_{\ell\to\ell'}^{\text{Purcell},\downarrow} = \sum_{n,n'} & P_{\text{res}}(n)\kappa(n_{\text{th}}(-\omega_{\ell',n',\ell,n}) + 1) \\ & \times \left| \left\langle \overline{\ell', n'} \middle| a \middle| \overline{\ell, n} \right\rangle \right|^2, \end{aligned} \tag{3.23}$$

for downward transitions.

The direct Purcell loss ($|e\rangle \rightarrow |g\rangle$) gives a T_1 limit $\sim$ 100 ms, effectively negligible in our experiments. However, heating to the excited levels of fluxonium due to the finite bath temperature, results in enhanced Purcell loss. Some of these states ($8^{\text{th}}, 9^{\text{th}}$ and 10^{th} eigenstates) have transition frequencies from the logical manifold that are close to the resonator frequency, resulting in avoided crossings. While their exact location depends sensitively on the circuit parameters, these resonances are likely responsible for the decreased T_1 observed near 0.35 Φ_0. The total Purcell relaxation rate for a bath temperature of 60 mK corresponds the dotted blue curve in Fig. 3.6.

3.4 Qubit dephasing measurement and analysis

The dephasing is characterized using a Ramsey sequence with three echo π pulses, and found to be minimized at $\Phi_{\text{ext}} = \Phi_0/2$, where the qubit frequency is first-order insensitive to changes in flux. The dephasing rate near the flux-frustration point can be separated into two parts. The first is a frequency-independent term Γ_C mainly composed of qubit depolarization, and dephasing from cavity photon shot noise and other flux insensitive white noise sources. The second arises from $1/f$ flux noise that is proportional to the flux slope as $\Gamma_{1/f} = \frac{d\omega}{d\Phi_{ext}}\eta\sqrt{W}$, where η is in the flux-noise amplitude and W depends on the number of π pulses in an echo experiment ($W = 4\ln 2 - \frac{9}{4}\ln 3$ for three π pulses Ithier et al. [2005]). Thus, our spin-echo signal decays as $\exp(-t/T_C) \times \exp(-\Gamma_{1/f}^2 t^2)$. Here $T_C = 1/\Gamma_C$ is the T_{2e} value at the flux-frustration point. It is found to be $\sim$ 300 μs, much higher than the T_{2e} values for state-of-the-art transmons, see inset of Fig. 3.7. The T_2^* was found to be $\sim 70 - 100$ μs, indicating that the dephasing is limited by low frequency flux noise. The T_{2e} values around the flux-frustration point, defined as the time for the echo oscillation amplitude to decay to $1/e$ are shown in Fig. 3.7. This value falls off rapidly as we move away from the flux-frustration point, consistent with the small tunnel coupling between levels. Away from the flux-frustration point, T_{2e} is mainly limited by $1/f$ flux noise. The T_{2e} far from

the frustration point is projected to be ~ 10 μs according to our model, which is consistent with other reported results Nguyen et al. [2019].

On the flux slope, the decay envelope of a Ramsey experiment is best approximated by a gaussian $\exp(-t^2/T_\phi^2)$, where $T_\phi = \Gamma_\phi^{-1} = (\sqrt{2}\eta(\partial_\phi\omega_{01})\sqrt{\ln\omega_{ir}t})^{-1}$ to first order. For the spin-echo experiments, low-frequency noise has a reduced weight in the noise spectrum, with $T_\phi = (\sqrt{W}\eta(\partial_\phi\omega_{01}))^{-1}$. We can calculate W for three echo π pulses based on Ithier et al. [2005]. At the flux frustration point, the qubit is first order insensitive to $1/f$ flux noise, and the spin-echo data can be explained with an exponential decay from white noise ($T_{2e} = T_C = \Gamma_C^{-1}$). In the regime of our spin-echo flux sweep, both noise sources contribute significantly. The data is therefore fit to a product of a gaussian and an exponential Groszkowski et al. [2018], with the T_{2e} defined as $\exp(-T_{2e}/T_C - T_{2e}^2/T_\phi^2) = 1/e$, i.e.,

$$T_{2e} = \frac{\sqrt{1/T_C^2 + 4/T_\phi^2} - 1/T_C}{2/T_\phi^2}. \tag{3.24}$$

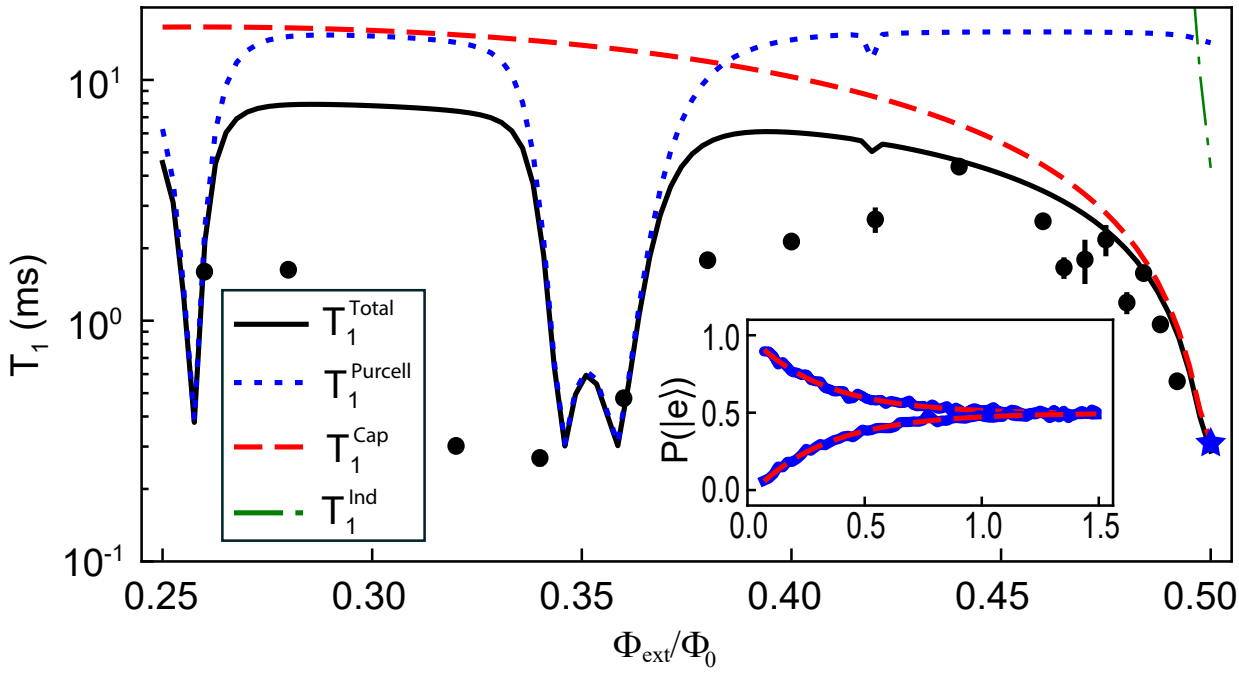

Figure 3.6: **Energy relaxation time (T_1) as a function of external flux, denoted by black circles.** The lines represent theoretical limits set by dielectric (T_1^{Cap}), inductive (T_1^{Ind}), Purcell (T_1^{Purcell}), and the combined loss (T_1^{Total}). The inset shows the decay of $P(|e\rangle)$ to 0.495 after preparing the qubit in $|g\rangle$,$|e\rangle$ at the flux-frustration point ($\star$).

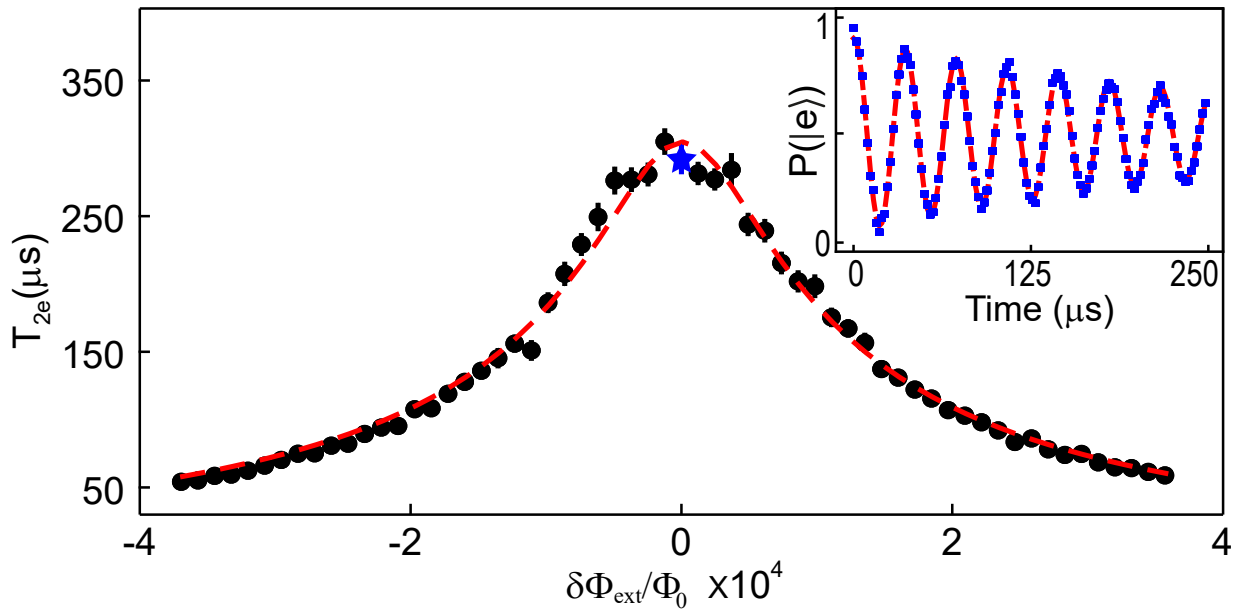

Figure 3.7: **Echo decay time T_{2e} as a function of flux near the flux-frustration point.** The inset shows an echo measurement at the flux-frustration point ($\star$).

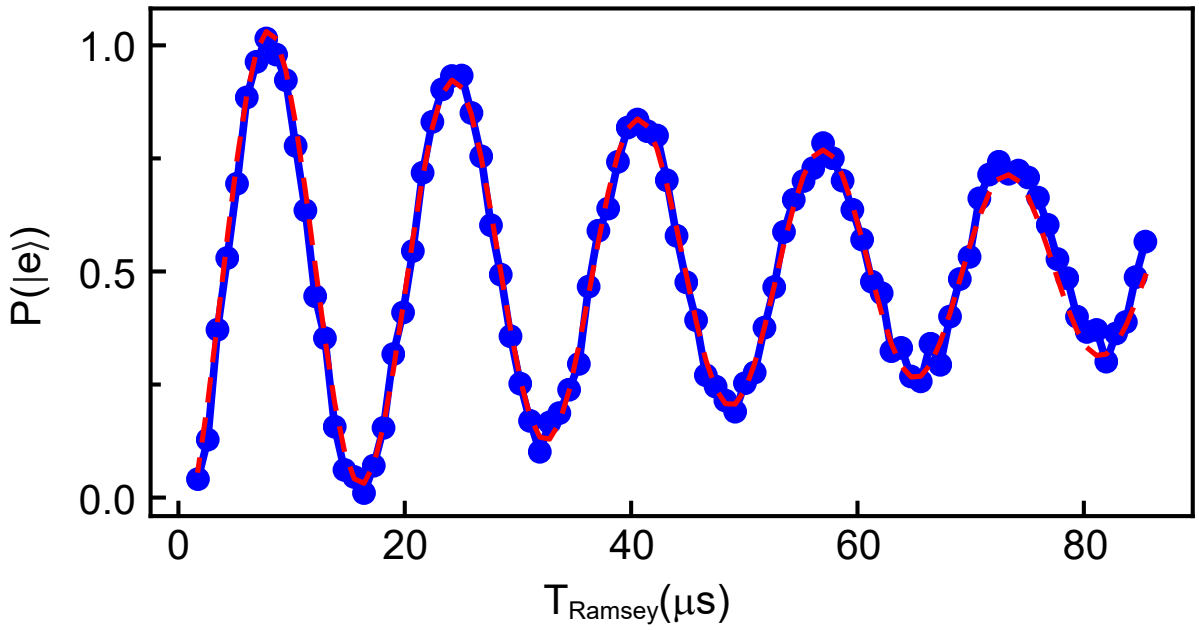

Figure 3.8: **Ramsey experiment at the flux-frustration point.** The T_2^* obtained by fitting the decay to an exponential is 71.3 μs.

CHAPTER 4

EXPERIMENT SETUP

Both single and two qubit experiments was performed in a Bluefors LD-250 dilution refrigerator with the wiring configured as shown in Fig. 4.2. The flux and charge inputs are attenuated at the 4 K stage and the mixing chamber with standard XMA attenuators, except the final 20 dB attenuator on the RF charge line (threaded copper). The DC and RF-flux signals were combined in a modified bias-tee (Mini-Circuits® ZFBT-4R2GW+), with the capacitor replaced with a short. The DC and RF-flux lines included commercial low-pass filters (Mini-Circuits®) as indicated. The RF flux and output lines also had additional low-pass filters with a sharp cutoff (8 GHz) from K&L microwave. Eccosorb (CR110) IR filters were added on the flux, input and output lines, which helped improve the T_1 and T_2 times, and reduce the qubit and resonator temperatures. The device was heat sunk to the base stage of the refrigerator (stabilized at 15 mK) via an OFHC copper post, while surrounded by an inner lead shield thermalized via a welded copper ring. This was additionally surrounded by two cylindrical μ-metal cans (MuShield), thermally anchored using an inner close fit copper shim sheet, attached to the copper can lid. We ensured that the sample shield was light tight, to reduce thermal photons from the environment.

We used the Xilinx FPGA board RFsoc ZCU111 as our Arbitrary Waveform Generator (AWG), which handles all the readout pulses, flux modulation pulses, and real time feedback. The board has two ADC channels with digital downmixing, thus we also use it for readout. We used YOKOGAWA DC power supplies as the current sources for DC flux bias of the fluxonium qubits and tunable coupler. The readout pulses at around 7GHz was upmixed with a 1GHz pulse from the ZCU111, and a constant RF signal at 8GHz from the Signalcore RF source. We also had bandpass filters and YIG filters on the readout lines to suppress all frequency components except the readout frequency.

We have 20dB attenuation at room temperature on the RF flux lines of the fluxonium

qubits, and 13dB attenuation on the RF flux line of the tunable coupler. We also have inner and outer DC blocks on all the control lines to completely separate the ground of the dilution refrigerator from all instruments, and keep the fridge completely floating. There are custom made RC low pass filters on all DC flux lines from the YOKO, with 150Ω resisters and several mF capacitances, to make sure that the cut-off frequency is around 0.1Hz.

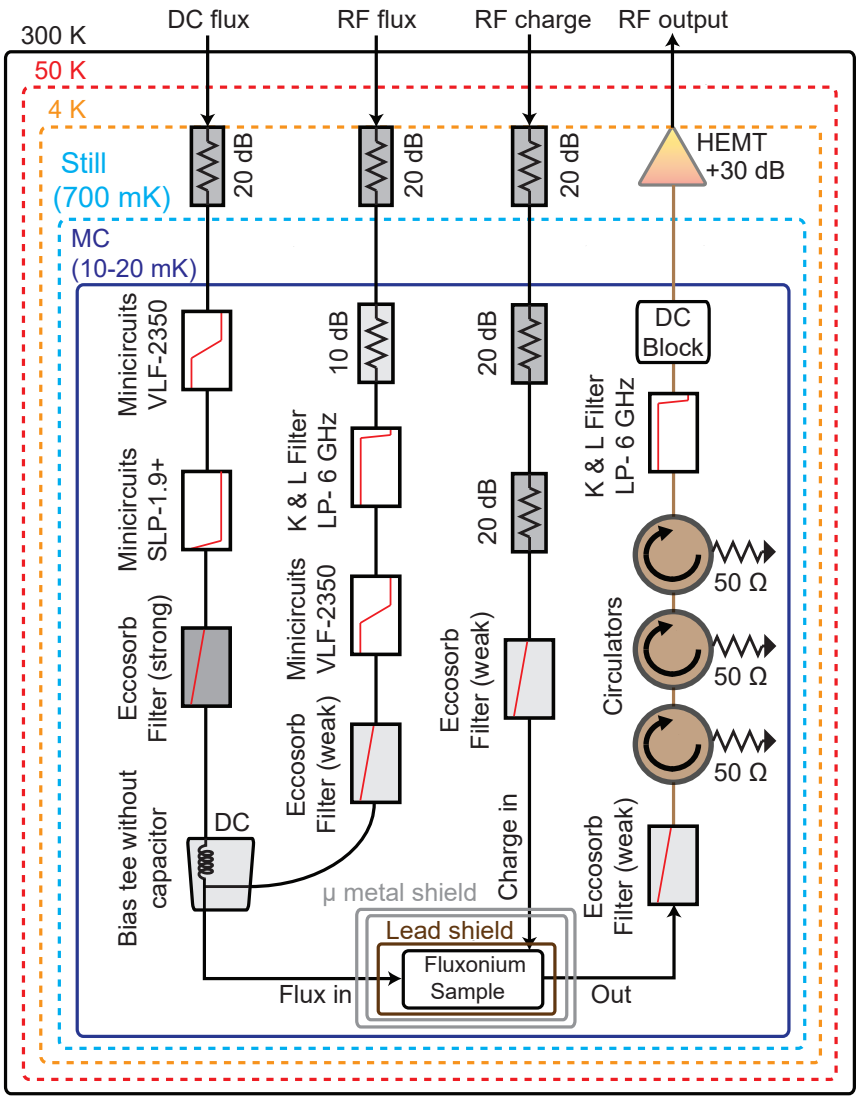

Figure 4.1: **Wiring diagram inside the dilution refrigerator.** Outside the dilution fridge, there is ~ 16 dB of attenuation and a DC block on the RF flux line, and an ultra low pass (~ 1 Hz) RC filter on the DC flux line. The total attenuation on the RF flux line proved important for both the T_1 and T_2 of the qubit, likely due to reduction in noise from the Arbitrary waveform generator (Agilent 81180A).

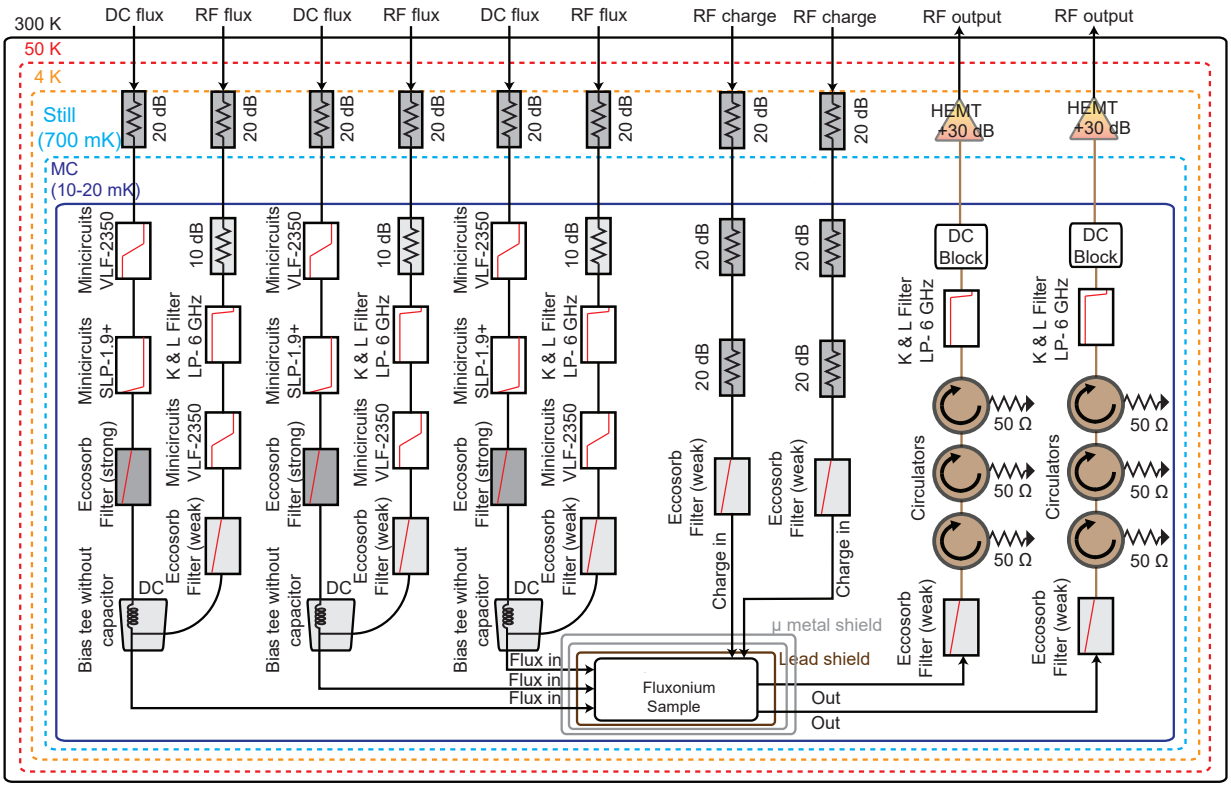

Figure 4.2: **Wiring diagram inside the dilution refrigerator.** Outside the dilution fridge, there is $13 - 20$ dB of attenuation and a DC block on the RF flux line, and an ultra low pass (< 1 Hz) RC filter on the DC flux line. The total attenuation on the RF flux line proved important for both the T_1 and T_2 of the qubit, likely due to reduction in noise from the Arbitrary waveform generator (Xilinx RFsoc).

CHAPTER 5

QUBIT INITIALIZATION AND READOUT

5.1 Initialization by Λ drive

Due to its low transition frequency, the qubit starts in a nearly evenly-mixed state in thermal equilibrium. We first initialize the qubit in a pure state ($|g\rangle$ or $|e\rangle$) using the reset protocol shown in Fig. 5.1, similar with Manucharyan et al. [2009], Magnard et al. [2018]. In this protocol, we simultaneously drive both the $|g0\rangle \rightarrow |h0\rangle$ and $|h0\rangle \rightarrow |e1\rangle$ transitions for 15 μs. The high resonator frequency (5.7 GHz) in comparison to the physical temperature, and the low resonator quality factor $Q = 600$ result in the rapid loss of a photon from $|e1\rangle$, effectively removing the entropy from the qubit. In conjunction with the large matrix element between $|h0\rangle$ and $|e1\rangle$, this steers the system into a steady state with $\sim 97\%$ of the population settling in $|e0\rangle$ in 15 μs (see Fig. 5.2). We subsequently perform an additional π pulse on the $|g\rangle - |e\rangle$ transition to initialize the system in the ground state ($|g0\rangle$). The reset is characterized by performing a Rabi rotation between the $|e\rangle \leftrightarrow |f\rangle$ levels, as shown in Fig. 5.1. The Rabi contrast is doubled following reset, consistent with $\sim 50\%$ of the population being in $|e\rangle$ in thermal equilibrium. If we prepare the system in $|g\rangle$, the $|e\rangle \leftrightarrow |f\rangle$ Rabi contrast indicates a $3 \pm 2\%$ error in state preparation, depending on the $|f\rangle$ state thermal population. Since the $|f\rangle$ frequency is similar to the typical transmon frequencies, its thermal population is in line with that of most transmons. The effective qubit temperature following reset is ~ 190 μK, lower than the ambient temperature by a factor of 100.

We derive the charge drive transition rates by simulating the full qubit-resonator dressed system. The drive power is normalized to 258 MHz so that the $|g0\rangle \rightarrow |h0\rangle$ π pulse takes 80 ns, which corresponds to the typical experimental value. The simulated single-photon and two-photon transition rates (in MHz) are shown in Table 5.1 and Table 5.2. The observed transition rates have additional contributions arising from the frequency dependence of the

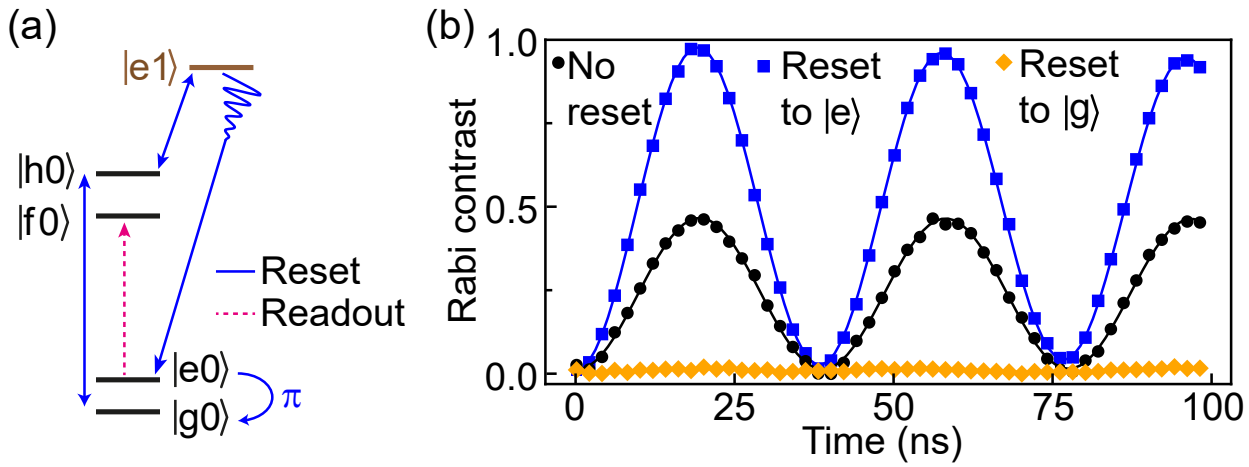

Figure 5.1: **Reset and readout schemes and measurements.** (a) Level diagram for the reset and readout protocols, where the letters g, e, f, h denote qubit energy levels and the numbers 0, 1 denote resonator levels. Reset is performed by simultaneously driving both $|g0\rangle \rightarrow |h0\rangle$ and $|h0\rangle \rightarrow |e1\rangle$ transitions (blue double-headed arrows). The spontaneous photon decay $|e1\rangle \rightarrow |e0\rangle$ provides a directional transition (blue single-headed arrow), removing the entropy and completing the reset. An $|e0\rangle \rightarrow |f0\rangle$ π pulse is applied before the readout to boost the output signal. (b) Rabi oscillations between $|e\rangle$ and $|f\rangle$ for different initial state preparations. Black circles: the initial state is the thermal equilibrium state. Blue squares: the initial state is prepared in $|e\rangle$ before the $|e\rangle \leftrightarrow |f\rangle$ Rabi. Orange diamonds: the initial state is prepared in $|g\rangle$.

Table 5.1: **Single-photon matrix elements**

	$\|g0\rangle$	$\|e0\rangle$	$\|f0\rangle$	$\|h0\rangle$	$\|g1\rangle$	$\|e1\rangle$
$\|g0\rangle$		0.0738		6.2577	257.9425	
$\|e0\rangle$	0.0738		5.8679			257.9108
$\|f0\rangle$		5.8679		1.2475	0.0138	
$\|h0\rangle$	6.2577		1.2475			0.1028
$\|g1\rangle$	257.9425		0.0138			0.0741
$\|e1\rangle$		257.9108		0.1028	0.0741	

transmission through the drive line.

Table 5.2: **Two-photon matrix elements** $\times 10^3$

	$\|g0\rangle$	$\|e0\rangle$	$\|f0\rangle$	$\|h0\rangle$	$\|g1\rangle$	$\|e1\rangle$
$\|g0\rangle$			1.9213			0.9177
$\|e0\rangle$				1.6489	0.4207	
$\|f0\rangle$	1.9213					0.0644
$\|h0\rangle$		1.6489			0.1258	
$\|g1\rangle$		0.4207		0.1258		
$\|e1\rangle$	0.9177		0.0644			

We utilized the $|g0\rangle \rightarrow |h0\rangle$ and $|h0\rangle \rightarrow |e1\rangle$ transitions for the reset protocol due to their large matrix elements. In principle, any transition combination that leads to fast, unidirectional population transfer can be used as the reset transitions. We chose the protocol based on the strength of the coupling between different states, and the detailed level structure for fastest reset. The excited state population as a function of reset time is shown in Fig. 5.2. The majority of the population is pumped to state $|e\rangle$ in 5 μs, which is mainly determined by the $|h0\rangle \rightarrow |e1\rangle$ transition rate. The reset process continues for another 10 μs until the steady state (97% in $|e\rangle$) is reached. We subsequently perform an additional π pulse on the $|g\rangle - |e\rangle$ transition to initialize the system in the ground state $|g0\rangle$.

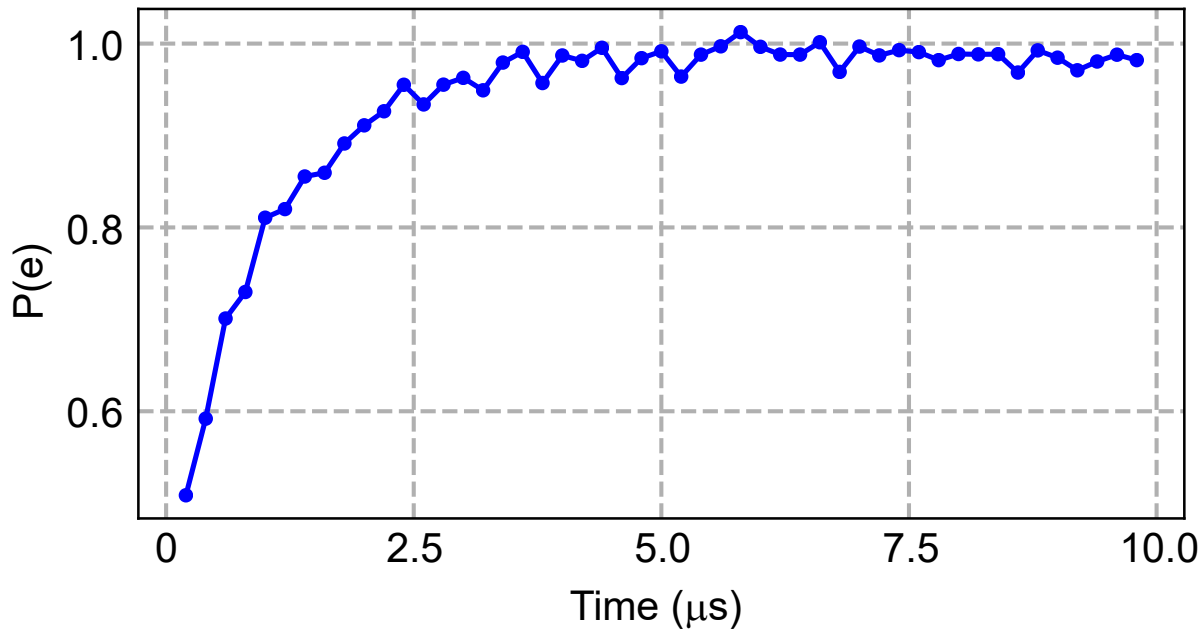

Figure 5.2: **The population in the $|e\rangle$ state as a function of the length of the reset pulse.** The population is measured after simultaneously driving the $|g0\rangle \rightarrow |h0\rangle$ and $|h0\rangle \rightarrow |e1\rangle$ transitions for different lengths of time. Reset of the state is achieved in ~ 5 μs.

5.2 Readout and active feedback

Readout of the fluxonium levels is performed using circuit QED Wallraff et al. [2004] by capacitively coupling the fluxonium circuit to a readout resonator Zhu et al. [2013]. Since the qubit states are far away in frequency from the readout resonator, the dispersive shift χ of the resonator due to a change in the occupation of computational states is small (60 kHz). Therefore, while the large detuning reduces the qubit heating through the resonator, it makes direct dispersive readout challenging. We circumvent this issue by utilizing the larger dispersive interactions χ_f, χ_h of the excited levels $|f\rangle$, $|h\rangle$, which are closer in frequency to the readout resonator. We thus perform a π pulse on the $|e\rangle - |f\rangle$ transition in 80 ns, before standard dispersive readout. Since the population in $|e\rangle$ is transferred to $|f\rangle$, the readout signal becomes proportional to $(\chi_f - \chi_g)$, which is 5 times larger than $(\chi_e - \chi_g)$. A previously reported dispersive shift engineering technique Manucharyan et al. [2009] for fluxoniums tried to increase $(\chi_e - \chi_g)$, while our protocol uses state selective transfer and

the dispersive shift between the excited plasmon states and the computational states for readout. This plasmon-assisted readout scheme results in 50% single-shot readout fidelity, which can be further improved with a parametric amplifier, and by optimizing the resonator κ and the dispersive shifts.

The resonator frequency shifts in increasing order are $\chi_e, \chi_g, \chi_h, \chi_f$. We selected the $|g\rangle, |f\rangle$ states for plasmon assisted readout since $\chi_f - \chi_g$ is larger than $\chi_h - \chi_e$. This is reflected in the single-shot readout histogram data for $|g\rangle, |e\rangle, |f\rangle, |h\rangle$ as shown in Fig. 5.3. The histograms are not well separated since the current sample is not optimized for high-fidelity readout. There are several avenues for further increasing the readout fidelity. The dispersive shifts of the plasmon levels can be increased by engineering the device parameters to bring some excited circuit levels closer to those of the resonator. We can further optimize readout by exploring different flux bias points to take full advantage of the meta stability of the fluxon. Lastly, the rich excited state spectrum allows for the use of different excited states for population transfer and dispersive shift engineering.

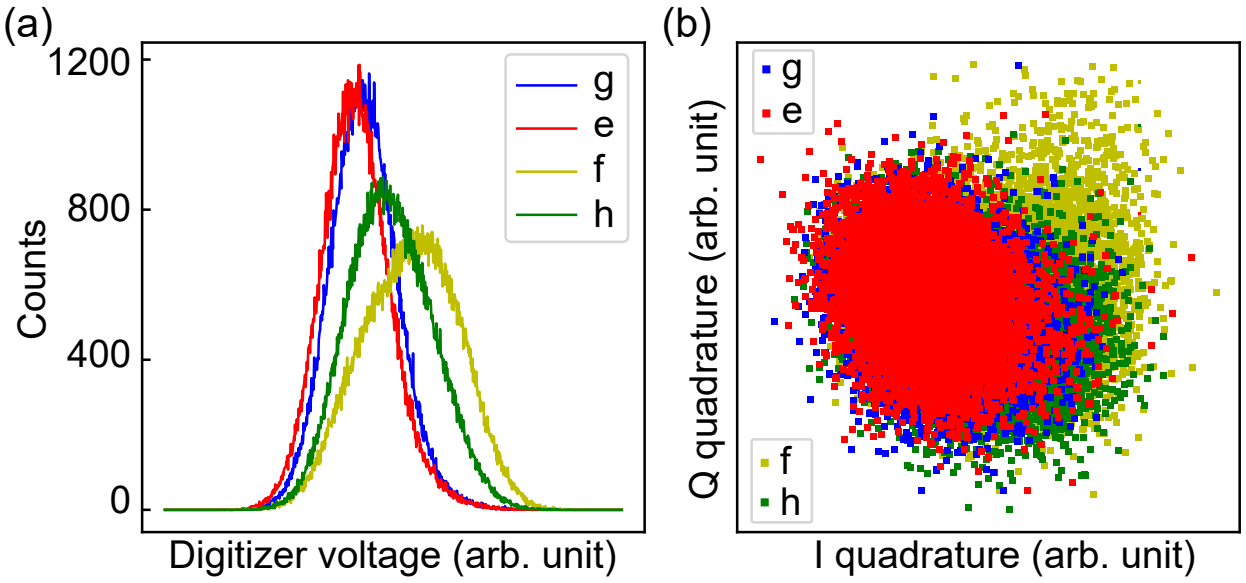

Figure 5.3: **Readout histogram and single shot data.** (a) histogram of the lowest 4 fluxonium states ($|g\rangle$,$|e\rangle$,$|f\rangle$,$|h\rangle$). The $|g\rangle$-$|f\rangle$ readout fidelity is $\sim 50\%$. (b) The distribution of all single shot data from the lowest 4 fluxonium states on the IQ plane.

By carefully engineering the qubit and readout resonator, we can significantly improve the χ/κ ratio for the fluxonium qubits, and achieve much better readout fidelity. We designed resonator line width $\kappa \approx 100$ kHz, and the computational levels have dispersive shift $\chi \approx$ 200kHz. With the two fluxonia device, we realized readout fidelity of 95% without any JPA or TWPA. With high readout fidelity, we can perform state initialization and reset with active feedback, which is demonstrated on the Xilinx RFsoc. We achieved state initialization fidelity close to the readout fidelity at around 95%.

CHAPTER 6

FAST SINGLE QUBIT GATES

6.1 Landau-Zener transition gate

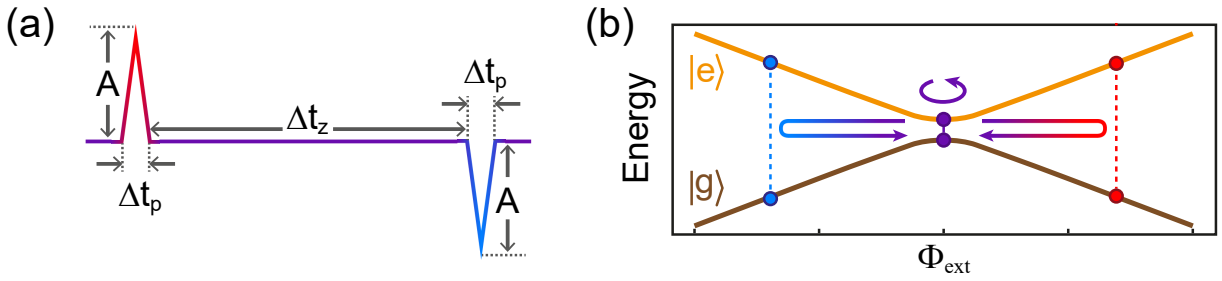

Figure 6.1: **Generic pulse scheme, gate calibration and performance.** (a) We use net-zero flux pulses as building blocks for universal control pulses. They are constructed using three sections, a positive triangular pulse with amplitude A and width Δt_p on the fast-flux line, an idling period of Δt_z and finally another triangular pulse identical to the first one but with a negative amplitude. (b) Energy levels of the computational space as a function of external flux (Φ_{ext}) showing how the fast-flux pulse changes the energies of the instantaneous eigenstates.

In order to maximize the advantage of the large anharmonicity of the heavy-fluxonium, we rethink the standard microwave-drive control of the circuit which is hindered by the suppressed charge matrix elements. We instead control the qubit through fast flux pulses, and report the first use of non-adiabatic Landau-Zener transitions to realize ultra-fast gates that occur within a single Larmor period. Near the flux-frustration point where the fluxonium is operated, the Hamiltonian within the computational space can be idealized as a spin-1/2 system, $\frac{H}{h} = \frac{A(\Phi_{\text{ext}})}{2}\sigma_x + \frac{\Delta}{2}\sigma_z$. Here $\Delta \approx 14$ MHz is the splitting of $|g\rangle$ and $|e\rangle$ at the flux-frustration point, and corresponds to the qubit frequency. The amplitude of the σ_x term is proportional to the flux offset $\delta\Phi_{\text{ext}}$ from the flux-frustration point, and given by $A = 4\pi\langle g|\hat{\varphi}|e\rangle(E_L/h)(\delta\Phi_{\text{ext}}/\Phi_0)$. The coefficient of the σ_x term can be much larger than the qubit frequency, with A $\sim$ 300 MHz when $\delta\Phi_{\text{ext}} = 0.06\Phi_0$, disallowing any rotating wave approximation.

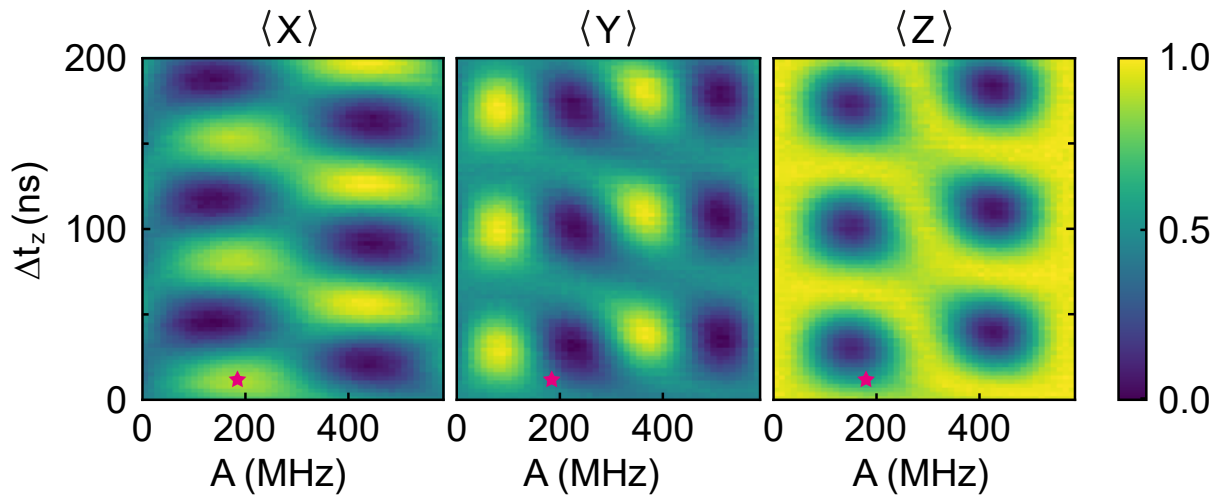

Figure 6.2: **Expectation values of σ_x, σ_y, and σ_z as a function of pulse parameters Δt_z and A.** These 2D sweeps are used to determine the optimal parameters for the $Y/2$ and arbitrary Z gates. $\star$ indicates the parameters for a $Y/2$ gate.

Fig. 6.1 shows the protocol for a generic qubit pulse. We first rapidly move the flux-bias point away from the flux-frustration point in one direction and back, thus generating a rotation about the x axis through a large σ_x term in our computational basis. There is additionally a relatively small rotation about the z axis corresponding to the time Δt_p of the triangular spike. We subsequently idle at the flux-frustration point for a duration Δt_z, which results in a rotation by $\omega_q \Delta t_z$ about the z axis. Finally, we rapidly move the flux-bias point in the other direction and back, resulting in a -σ_x term and another small z rotation. We choose the two spikes to be exactly anti-symmetric, ensuring zero net flux, simultaneously minimizing the effect of microsecond and millisecond pulse distortions ubiquitous in flux-bias lines Rol et al. [2019], and echoing out low-frequency noise. The pulse is also immune to shape distortions since the total σ_x and σ_z amplitudes depend only on the area of the spike and Δt_z. By sweeping the amplitude A of the triangular spike and idling length Δt_z of the pulse, and measuring the expectation value of the spin along each axis, we obtain the 2d Rabi patterns shown in Fig. 6.2 that provide a measure of our gate parameters. A vertical line cut of these graphs corresponds to Larmor precession in the lab frame, with an oscillation

frequency of $\Delta = 14$ MHz. We thus obtain a $Z/2$ gate by idling at the flux-frustration point for $\Delta t_z = 1/(4\Delta)$. We obtain a $Y/2$ gate at the point indicated by the red star, with the corresponding trajectories on the Bloch sphere for three different cardinal states shown in Fig. 6.3. $Y/2$ and arbitrary rotations about the z axis are sufficient for generating any single qubit unitary, thus realizing universal control. An $X/2$ gate, for instance, is performed through the combination $(-Y/2) \cdot (Z/2) \cdot (Y/2)$.

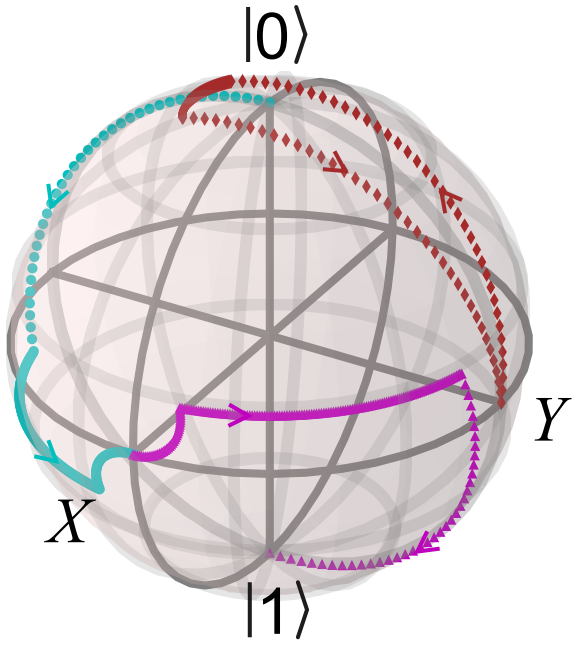

Figure 6.3: **Trajectories of three distinct initial states** $|0\rangle$ (cyan), $(|0\rangle + |1\rangle)/\sqrt{2}$ (magenta) and $(|0\rangle + i|1\rangle)/\sqrt{2}$ (brown) on the Bloch sphere when a $Y/2$ gate is applied.

We characterize the fidelities of our single-qubit gates through randomized benchmarking (RB) Knill et al. [2008], Chow et al. [2009] and interleaved RB (IRB) Magesan et al. [2012]. RB provides a measure of the average fidelity of single-qubit Clifford gates and is performed by applying sequences containing varying number of Clifford gates on the state $|e\rangle$. For a given sequence length, we perform 75 randomized sequences, each containing a recovery gate to the state $|e\rangle$ before the final measurement. IRB allows us to isolate the fidelities of individual computational gates and is performed by interleaving the gate between the

random Clifford gates of the RB sequence. The averaged decay curves of $P(|e\rangle)$ as a function of the sequence length for standard RB (black circles), and IRB for $Z/2$ (red triangles), $Y/2$ (gold diamonds) and $X/2$ (cyan squares) gates are shown in Fig. 6.4. The infidelities thus extracted for the $Y/2$, $Z/2$, and $X/2$ gates are $8, 1,$ and 24×10^{-4}, respectively. The $X/2$ gate infidelity is slightly worse than the combined infidelities from two $Y/2$, and one $Z/2$ gate. The durations for $Y/2$ and $Z/2$ are ~ 20 ns, while that for the $X/2$ gate is ~ 60 ns, and thus all the computational gates are performed within one qubit Larmor period $2\pi/\omega_q = 70$ ns, with all the operations occurring in the lab frame. The calculated decoherence limited errors of the $Y/2$, and $X/2$ gates are 6.67×10^{-5} and 2×10^{-4}, suggesting that the major source of gate error arises from residual calibration errors in the pulse parameters, providing room for improvement even from these state-of-the-art values.

6.2 Analytical description and numeric simulation

Modulation of the external flux drive with appropriate amplitude and duration is sufficient to perform arbitrary single-qubit rotations. The native gates available in our system are the arbitrary phase gate $R_z(\theta)$ which rotates the qubit by an arbitrary angle θ about the Z-axis and a combination of X- and Z-rotation $R_{xz}(\theta)$. $R_z(\theta)$ is realized by waiting for a period of $\Delta t_z = \theta/\omega_q$ (since we are working in the lab frame) whereas $R_{xz}(\theta)$ is implemented by a flux-drive applied for a duration of $\Delta t_p = \lambda\theta/\omega_q$. Here λ ($\lambda \leq 1$) is the ratio of Z-rotation to X-rotation rates. These rotation matrices can be expressed as,

$$R_z(\theta) = e^{-i\sigma_z\theta/2}, \tag{6.1}$$

$$R_{xz}(\theta) = e^{-i(\theta\sigma_x+\lambda|\theta|\sigma_z)/2}. \tag{6.2}$$

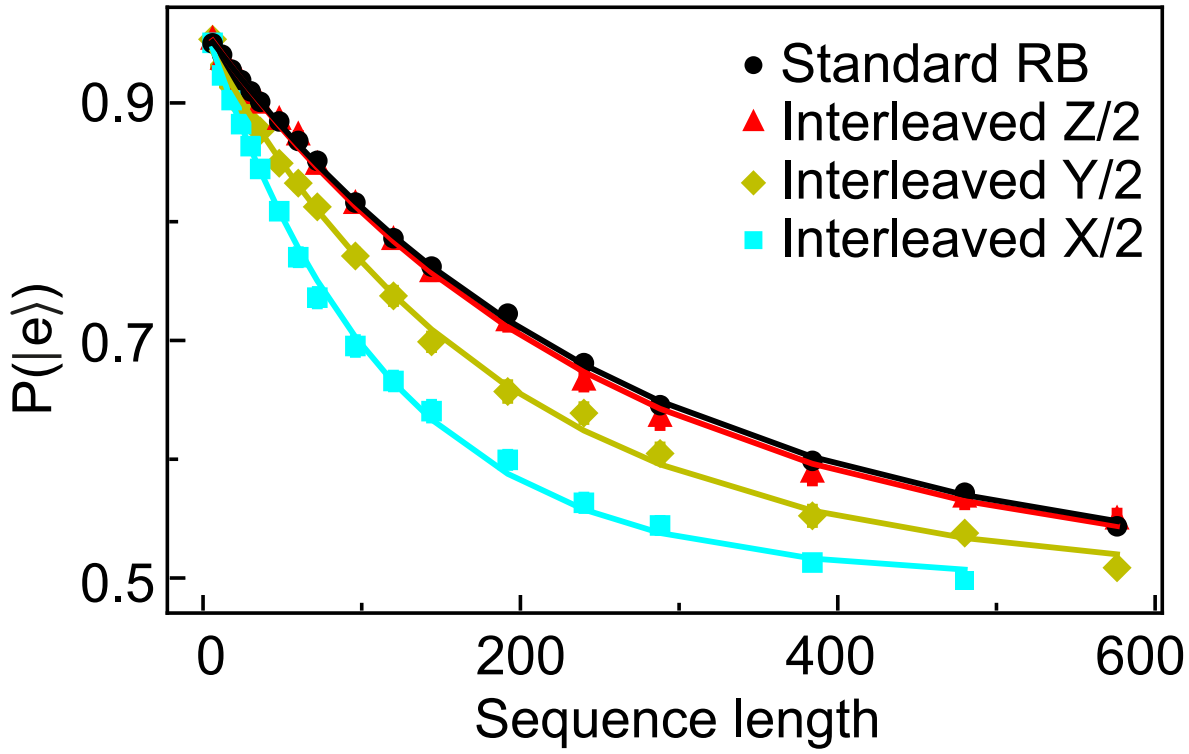

Figure 6.4: **Comparison of standard RB (black circles) and interleaved RB for $Z/2$ (red triangles), $Y/2$ (gold diamonds) and $X/2$ (cyan squares) gates.** The plot is a result of 75 randomized gate sequences averaged over 10000 times. The average gate fidelity is $\mathcal{F}_{\text{avg}} = 0.9980$ and the individual gate fidelities are $\mathcal{F}_{Z/2} = 0.9999$, $\mathcal{F}_{Y/2} = 0.9992$ and $\mathcal{F}_{X/2} = 0.9976$ Magesan et al. [2012]. The uncertainties in all fidelities are smaller than the least significant digit.

The $|\theta|$ in Eq. 6.2 arises due to the always-on Z-rotation which is unidirectional in the lab frame. A generic zero-flux-pulse can be constructed as,

$$R(\theta) = R_{xz}(-\theta_x) \cdot R_z(\theta_z) \cdot R_{xz}(\theta_x). \tag{6.3}$$

A $\pi/2$ rotation about the Y-axis ($Y/2$), i.e.,

$$R_y(\pi/2) = \frac{1}{\sqrt{2}} \begin{pmatrix} 1 & -1 \\ 1 & 1 \end{pmatrix}, \tag{6.4}$$

is obtained using,

$$\theta_x = \frac{1}{\sqrt{1+\lambda^2}} \cos^{-1}\left[\frac{\lambda(1+\lambda)}{-(1-\lambda)}\right], \tag{6.5a}$$

$$\theta_z = 2\tan^{-1}\left[\frac{\sqrt{1-2\lambda-2\lambda^3-\lambda^4}}{(1+\lambda)\sqrt{1+\lambda^2}}\right] \tag{6.5b}$$

in Eq. 6.3 provided $0 \leq \lambda \leq \sqrt{2}-1$. Similarly, we can construct

$$R_y(\pi) = \begin{pmatrix} 0 & -1 \\ 1 & 0 \end{pmatrix} = -i\sigma_y \tag{6.6}$$

using,

$$\theta_x = \frac{1}{\sqrt{1+\lambda^2}} \cos^{-1}(\lambda^2), \tag{6.7a}$$

$$\theta_z = \pi - 2\tan^{-1}\left[\frac{\lambda}{\sqrt{1-\lambda^2}}\right], \tag{6.7b}$$

with $0 \leq \lambda \leq 1$. An arbitrary rotation about X-axis can be constructed using,

$$R_x(\theta) = R_y(\pi/2) \cdot R_z(\theta) \cdot R_y(-\pi/2). \tag{6.8}$$

These gates are sufficient to construct any single-qubit unitary operation. We used the QuTiP Johansson et al. [2013] python package to simulate the evolution of the computational levels under application of the pulse that was shown in Fig. 6.1, and obtained the gate parameters. We swept the drive amplitude A and idling period Δt_z in our simulation to match the sweep performed in the experiment, as shown in Fig. 6.5. $\Delta t_p = 4.76$ ns in all the experiments and simulations reported in this paper.

A complete Clifford set includes the computational gates $(\exp\big(\pm i\pi\sigma_j/4\big),\ j = x, y)$ and the Pauli gates $(\exp\big(\pm i\pi\sigma_j/2\big),\ j = I, x, y, z)$. In this work, we constructed $Y/2$ and $Z/2$

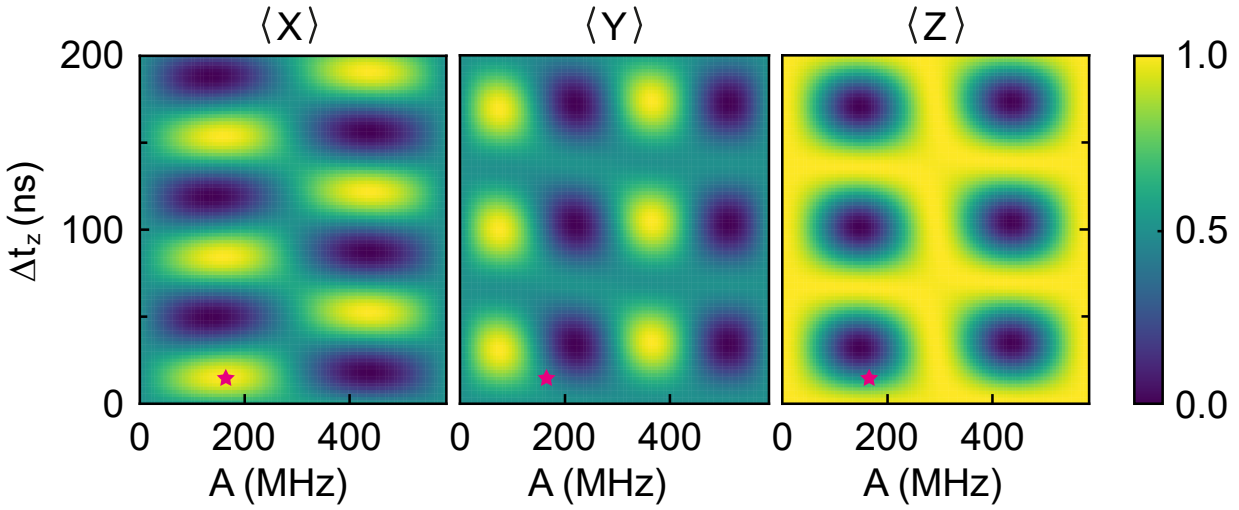

Figure 6.5: **Simulated expectation values of σ_x, σ_y and σ_z as a function of pulse parameters Δt_z and A with $\Delta t_p = 4.76$ ns.** The simulation shows extremely good agreement with the experimental data as shown in Fig. 6.2.

Table 6.1: **Clifford gates**

Gate	Length (ns)	Expm infidelity	Gate Composition
$Y/2$	21.19	8×10^{-4}	
$Z/2$	17.87	1×10^{-4}	
$X/2$	60.25	24×10^{-4}	$Y/2$, $Z/2$, $-Y/2$
Y	42.38		$Y/2$, $Y/2$
Z	35.73		$Z/2$, $Z/2$
X	78.11		$Y/2$, Z, $-Y/2$

gates, and used them as building blocks for the other gates in the Clifford Set. The total gate lengths, experimental infidelities (computational gates only), and gate compositions are shown in Table 6.1. The computational gate lengths range from $21 - 60$ ns, and the longest Pauli gate (X) has a length of 78 ns. Since $2\pi/\omega_q \approx 70$ ns, the computational gates are all within a single cycle of the qubit, and the longest gate is around one cycle as well. These single-cycle flux gates are $10 - 30$ times faster than standard microwave driven gates, whose durations are longer than $10 \times 2\pi/\omega_q$.

CHAPTER 7

TUNABLE INDUCTIVE COUPLER AND TWO QUBIT GATES

7.1 Tunable coupler

We design an inductively coupled tunable coupler for fast two qubit gates between heavy fluxonium qubits. The on-chip geometry of the device is shown in figure 3.2. The circuit Hamiltonian is $H = H_0 + V$, where

$$\begin{aligned} H_0 = &\sum_{\mu=a,b} [4E_{C\mu} n_\mu^2 + \frac{1}{2} E_L \varphi_\mu^2 - E_{J\mu} \cos\big(\varphi_\mu + \pi\big)] \\ &+ 4E_{C-} n_-^2 + \frac{1}{2} E_{Lc} \theta_-^2 - E_{Jc} \cos(\theta_- + \phi_c) \\ &+ 4E_{C+} n_+^2 + \frac{1}{2} E_{Lc} \theta_+^2, \end{aligned} \tag{7.1}$$

$$\begin{aligned} V = &-\frac{E_L}{2}[\varphi_a(\theta_+ + \theta_-) + \varphi_b(\theta_+ - \theta_-)] \\ &+ \sum_{\mu=a,b} \frac{E_L}{2} \delta\phi_\mu [-2\varphi_\mu + \theta_+ + (-1)^\mu \theta_-], \end{aligned} \tag{7.2}$$

where μ obeys the correspondence $a \to 0, b \to 1$ when appearing in an exponent. We define the inductive energy of the coupler $E_{Lc} = \frac{1}{2}(E_L + E_L')$, and the charging energies $E_{C\mu} = e^2/2C_\mu,\ \mu = a, b, E_{C+} = e^2/(2[C/2]), E_{C-} = e^2/(2[C_c + C/2])$, where the remaining circuit parameters can be read off from Fig. 3.3. The node variables φ_a, φ_b are the qubit variables, while the coupler variables are defined as $\theta_\pm = \varphi_1 \pm \varphi_2$. We have isolated the qubit-flux shifts away from the sweet spot $\delta\phi_\mu = \phi_\mu - \pi$, where $\phi_\mu = 2\pi\Phi_\mu/\Phi_0$ is the reduced external flux, Φ_μ is the external flux in the corresponding loop and $\Phi_0 = h/2e$ is the superconducting flux quantum.

Due to the very large frequency gap between the low-frequency computational levels and higher levels, we can reduce the Hamiltonian into the computational subspace that we are

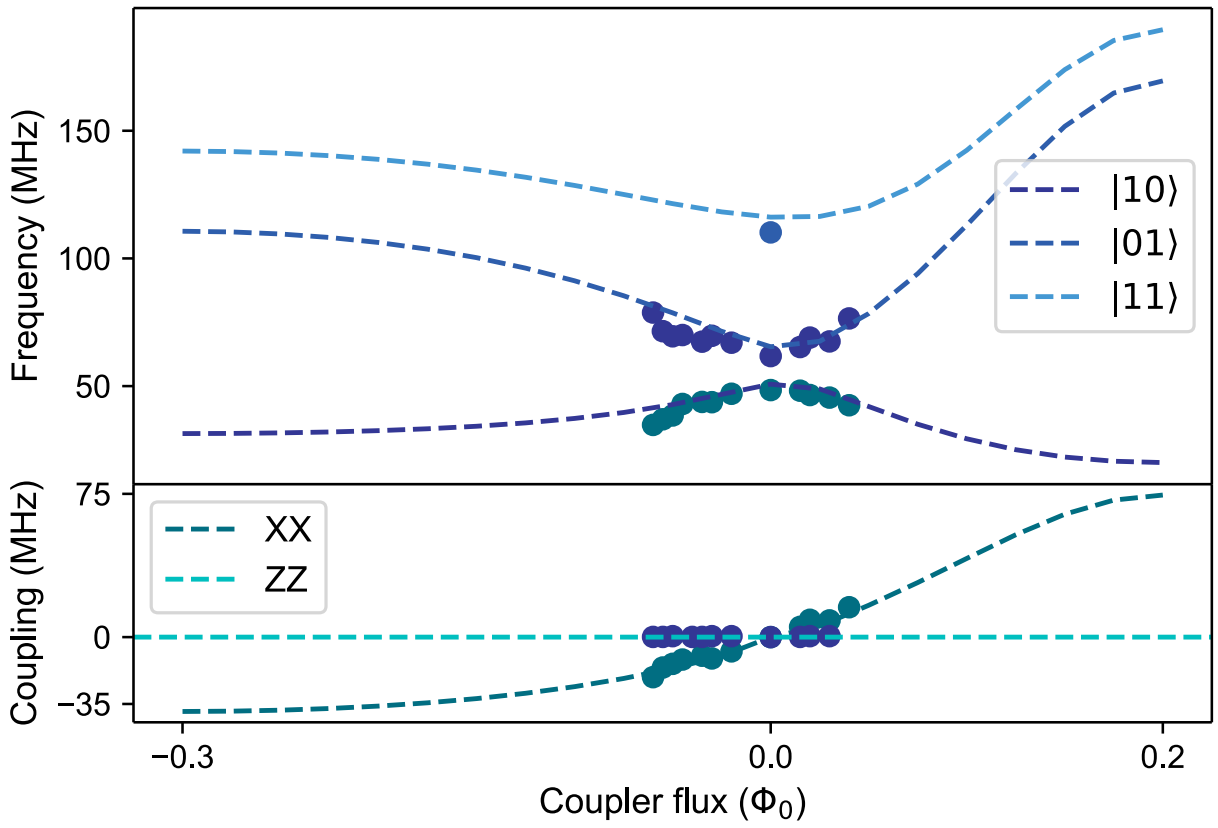

Figure 7.1: **Qubit frequencies and coupling vs coupler flux.** Top panel: $|01\rangle$, $|10\rangle$, and $|11\rangle$ state frequencies vs coupler flux. The qubits are always tuned to be at their sweet spots while sweeping the coupler flux bias. The dashed lines are from numeric simulations with parameters extracted from qubit spectroscopy. Bottom panel: XX and ZZ coupling strength calculated from the data and simulations. ZZ is < 0.1kHz across all coupler flux range.

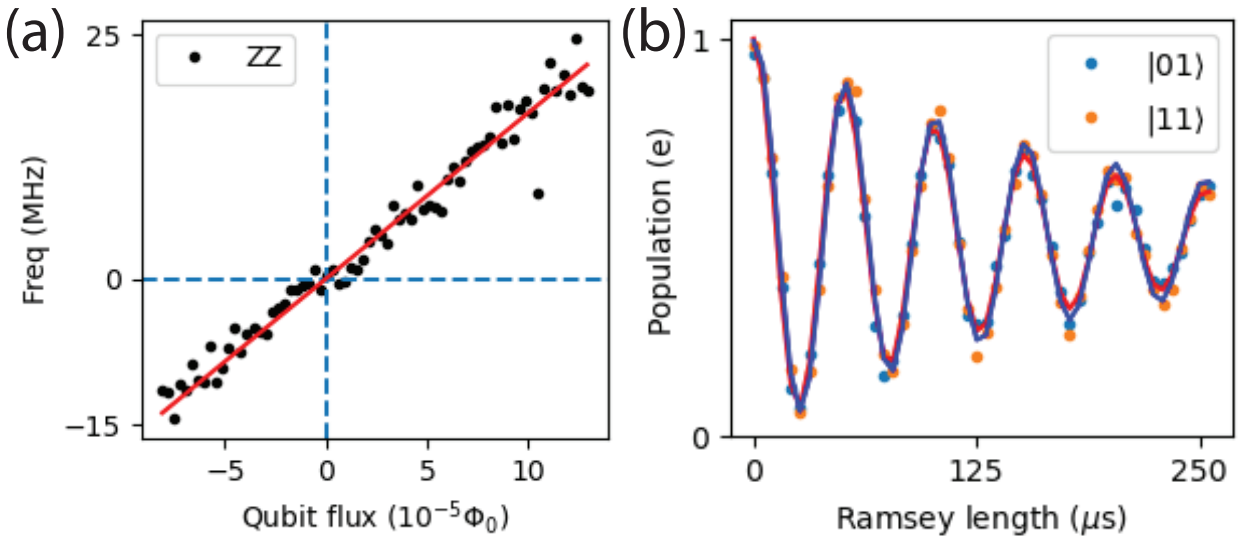

Figure 7.2: **ZZ measurement at and around the coupler off point.** (a) By sweeping the qubit fluxes around the coupler off point, ZZ will gain a nonzero value. (b) Ramsey experiment of qubit B at the coupler off point, with initial state $|01\rangle$ or $|11\rangle$. The frequency difference between the two Ramseys ($f_{11} - f_{10}$ and $f_{01} - f_{00}$) gives ZZ coupling strength < 0.1kHz.

most interested in

$$H_{\text{eff}} = -\sum_{\mu=a,b} \frac{\omega'_\mu}{2}\sigma_z^\mu + J\sigma_x^a\sigma_x^b - \sum_{\mu=a,b}\Omega_\mu\sigma_x^\mu. \tag{7.3}$$

The coupling is XX in our system, and we expect ZZ to be 0 across all coupler fluxes provided that the qubits are maintained at their sweet spots with appropriately adjusted flux biases.

Due to the property of this coupler, the coupler flux bias will introduce a small shift to the qubit sweet spot positions Weiss et al. [2022]. By sweeping the coupler flux while keeping both qubits at their sweet spots, we generated figure 7.1. The ZZ coupling term is negligible along this line, and we find the 0 XX coupling position at $\Phi_C = 0.3\Phi_0$, where $f_{01} - f_{10}$ is at its minimum. A nonzero ZZ coupling will be introduced when the qubits are not on their sweet spots, and we can utilize this property to fine tune our flux biases.

At the coupler off point, the qubit T_1s are 180μs and 300μs respectively, and qubit T_{2e}s

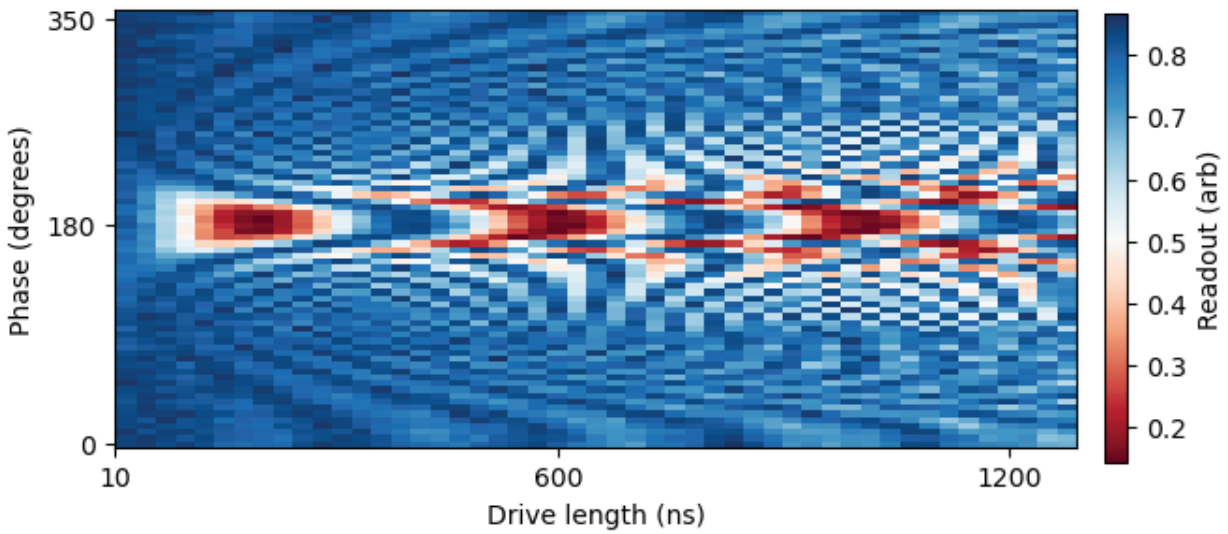

Figure 7.3: **Calibration data for phase of the cancellation pulse.** Performing a blue sideband drive at the desired frequency while sweeping the phase of a cancellation pulse. The amplitude of this sweep is randomly chosen, but it needs to be lower than the correct cancellation amplitude.

are 250μs and 300μs. The coherence of both qubits is very close to the uncoupled fluxonium qubits at similar frequencies, thus the coupler has almost no impact on the qubit coherence when it is turned off.

The full analytical study of this circuit with Schrieffer–Wolff transformation can be found in Weiss et al. [2022]. We start with the full Hamiltonian of the system and report simulation results from diagonalizing the full circuit with scQubitsGroszkowski and Koch [2021] open source python library. In the numerical study of two qubit dynamics, we simulate the system with all four modes - two fluxoniums coupled by a fluxonium and a linear resonator. Using the bare eigenstates of the uncoupled Hamiltonian in Eq. (7.1) as a set of basis, we first represent the Hamiltonian in the matrix form and then diagonalized the matrix to obtain the spectrum. Note that putting the terms proportional to the flux-bias $\delta\phi_\mu$ in the interaction part of the Hamiltonian in Eq. (7.2) will simplify numerical analysis near off position by keeping the eigenstates close to the bare states.

Perturbation theory reveals that a set of $\delta\phi_\mu$ and ϕ_c can place two qubits at their en-

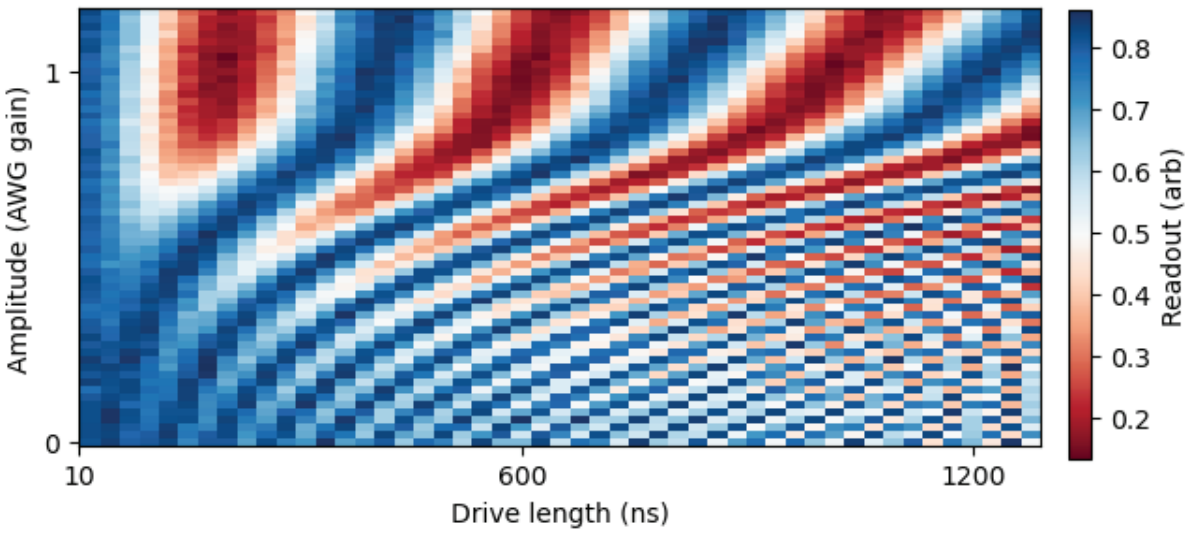

Figure 7.4: **Calibration data for the amplitude of the cancellation pulse.** Performing a blue sideband drive at the desired frequency while sweeping the amplitude of a cancellation pulse.

ergy sweet spot and make their effective coupling strength $J = 0$, referred to as the "off position". We can numerically locate the off position by minimizing the eigenenergy f_{11} of state $|\overline{11}\rangle$. Although the ZZ coupling strength is in general non-zero at the off position, small $\delta\phi_\mu$ adjustments can nullify ZZ. In practice, the adjustment amount can be found by minimizing $(f_{01} + f_{10} + |ZZ|)$ or $|ZZ|$ within a small range near the off position. Typically, the adjustments of both qubits' flux biases are on the order of $10^{-5}\Phi_0$ and bias the qubits away from their sweet spots. Such small adjustments modify the qubit frequencies by $\sim$ 5Hz and impose an upper bound of the pure dephasing time of $\sim$ 1ms, which is acceptable. For any other coupler flux value away from the off position, we are also able to use the similar strategy to find $\delta\phi_\mu$ that reduce ZZ coupling strength to zero. Utilizing the high tunability, our device is effectively freed from unwanted ZZ coupling while retaining XX coupling.

By appropriately allocating external fluxes in the Hamiltonian, we construct drive operators that correspond to three time-dependent external fluxes. Simulations of a closed system suggest that leakage to non-computational states is negligible, attributed to the significant detuning between the drive and the undesired transition frequency. Across all gates pre-

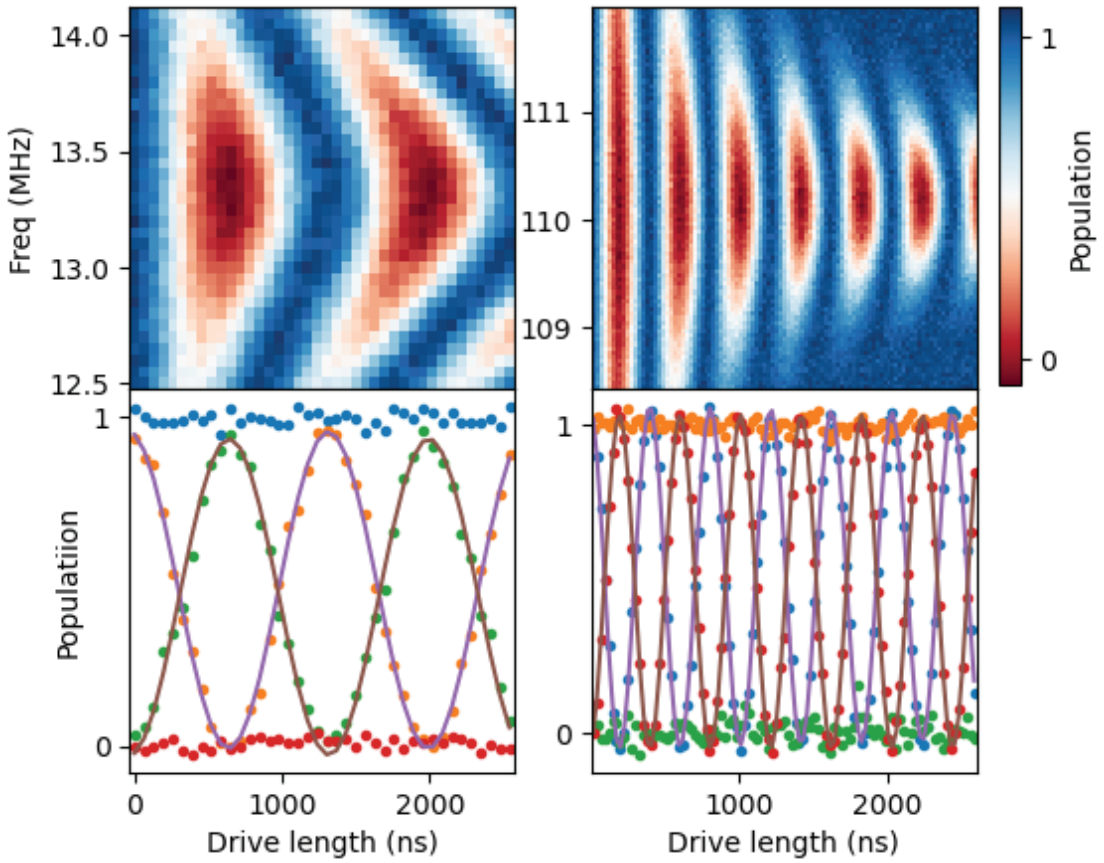

Figure 7.5: **Red sideband and blue sideband Chevron patterns.** (a) Top panel: Red sideband chevron centered around 13.3MHz. Bottom panel: correlated oscillation between $|01\rangle$ and $|10\rangle$, while $|00\rangle$ and $|11\rangle$ stay the same. A period of the oscillation takes 1300ns. (b) Top panel: Blue sideband chevron centered around 110.2MHz. Bottom panel: correlated oscillation between $|00\rangle$ and $|11\rangle$, while $|01\rangle$ and $|10\rangle$ stay the same. A period of the oscillation takes 400ns.

sented in this work, closed system simulations consistently report infidelities on the order of 99.999%. Upon transitioning to open system simulations, the infidelities of single qubit gates, $\sqrt{i\text{SWAP}}$, and $\sqrt{b\text{SWAP}}$ gates are reduced to 99.94%, 99.76%, and 99.92% respectively. Our numerical simulations suggest that gate fidelity is predominantly constrained by decoherence.

For readout simulations, we can ignore the contribution of coupler and the other qubit, and approximate the system as a fluxonium coupled to its corresponding readout resonator.

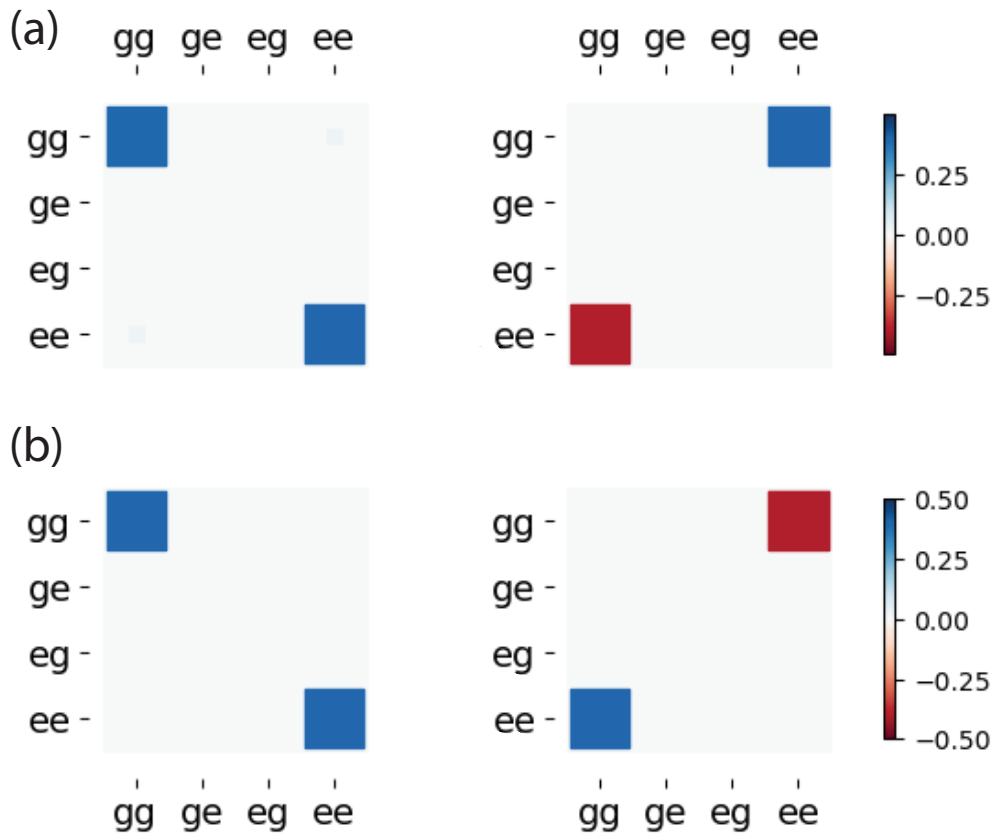

Figure 7.6: **State tomography of a $|gg\rangle + |ee\rangle$ Bell state prepared by the $\sqrt{b\text{SWAP}}$ gate.** (a) State tomography of the experimentally prepared Bell state. (b) State tomography of the ideal Bell state generated by simulation.

7.2 RF Crosstalk and Calibrations

Let us consider the case of RF flux crosstalk where flux penetrates each of the qubit loops when we drive the coupler. The Hamiltonian of the system after truncating to the computational manifold is

$$H = -\frac{\omega_a}{2}\sigma_{za} - \frac{\omega_b}{2}\sigma_{zb} + \alpha E_{La}\langle\phi_a\rangle_{01}\cos(\omega_d t)\sigma_{xa} \tag{7.4}$$
$$+\beta E_{Lb}\langle\phi_b\rangle_{01}\cos(\omega_d t)\sigma_{xb} + J_{\text{ac}}\cos(\omega_d t)\sigma_{xa}\sigma_{xb},$$

where α and β encode the amount of crosstalk from the coupler drive through the qubit loops and J_{ac} is given in Ref. Weiss et al. [2022]. The drive frequency will typically be set to

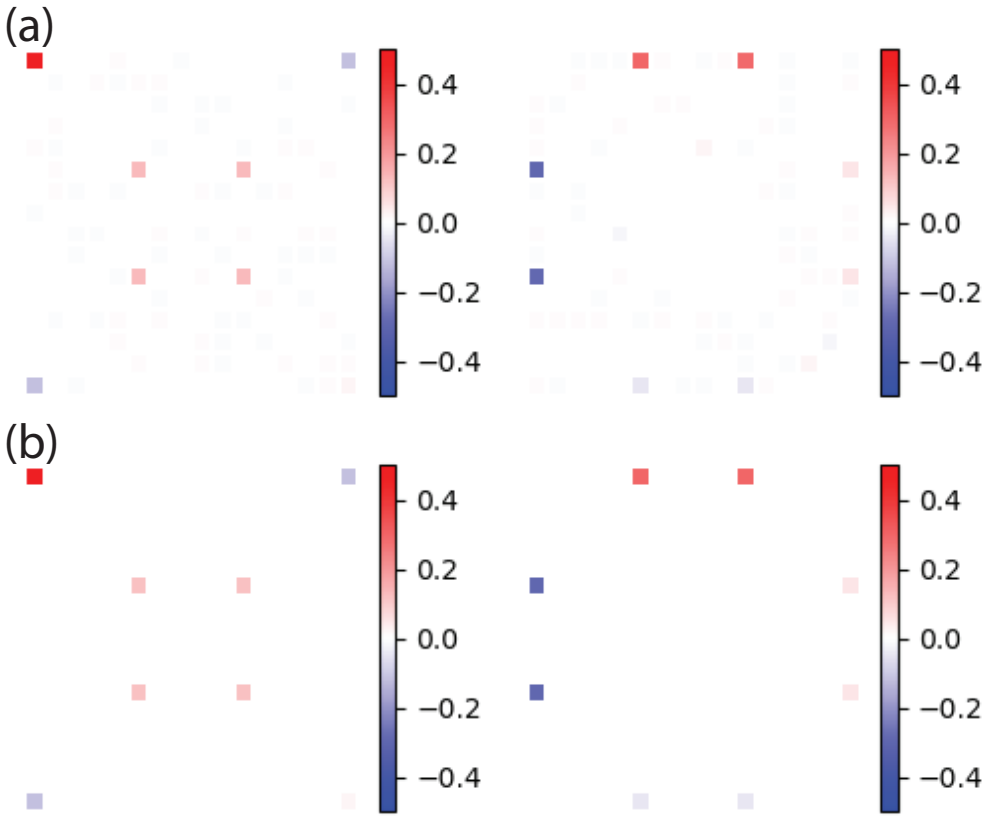

Figure 7.7: **Process tomography of the $\sqrt{i\text{SWAP}}$ gate.** (a) Experimentally measured χ matrices from process tomography of the $\sqrt{i\text{SWAP}}$ gate. (b) Ideal χ matrices from simulation.

$\omega_d \approx \omega_a - \omega_b$ for an iSWAP-style gate, or $\omega_d \approx \omega_a + \omega_b$ for a bSWAP-style gate. In each case, the single-qubit drives are detuned from single-qubit resonances. Thus the single-qubit drive terms act not to induce Rabi oscillations but instead to dynamically shift the frequencies of each qubit Blais et al. [2007]. To see this, we first move to a frame rotating at the drive frequency, defined by the unitary

$$U_1(t) = \exp\left(i\frac{\omega_d}{2}t\sigma_{za} + i\frac{\omega_d}{2}t\sigma_{zb}\right). \tag{7.5}$$

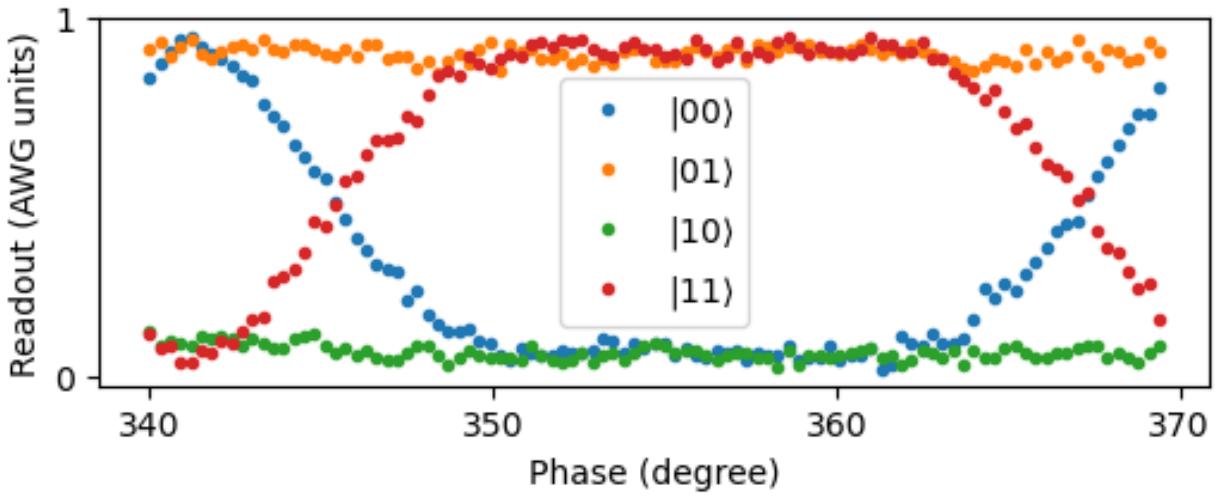

Figure 7.8: **Calibration data for ϕ_{11} measurement.** Performing a blue sideband drive at the desired frequency while sweeping the phase of a cancellation pulse. The amplitude of this sweep is randomly chosen, but it needs to be lower than the correct cancellation amplitude.

The new Hamiltonian is $H' = U_1^\dagger H U_1 - i U_1^\dagger \dot{U}_1$, yielding

$$\begin{aligned} H' = &-\frac{\omega_a - \omega_d}{2}\sigma_{za} - \frac{\omega_b - \omega_d}{2}\sigma_{zb} \\ &+ \frac{\alpha E_{La}\langle\phi_a\rangle_{01}}{2}\sigma_{xa} + \frac{\beta E_{Lb}\langle\phi_b\rangle_{01}}{2}\sigma_{xb} \\ &+ J_{\mathrm{ac}}\cos(\omega_d t)(\cos(\omega_d t)\sigma_{xa} + \sin(\omega_d t)\sigma_{ya}) \\ &\times (\cos(\omega_d t)\sigma_{xb} + \sin(\omega_d t)\sigma_{yb}), \end{aligned} \tag{7.6}$$

making the RWA for the single-qubit drive terms (which we are about to perturbatively eliminate) while keeping all terms associated with the two-qubit drive. We now eliminate the single-qubit drive terms to first order in the small parameters $\alpha E_{La}\langle\phi_a\rangle_{01}/(\omega_a - \omega_d), \beta E_{Lb}\langle\phi_b\rangle_{01}/(\omega_b - \omega_d) \ll 1$ by employing a Schrieffer-Wolff transformation effected by the unitary

$$U_2 = \exp\left(i\frac{\alpha E_{La}\langle\phi_a\rangle_{01}/2}{\omega_a - \omega_d}\sigma_{ay} + i\frac{\beta E_{Lb}\langle\phi_b\rangle_{01}/2}{\omega_b - \omega_d}\sigma_{by}\right), \tag{7.7}$$

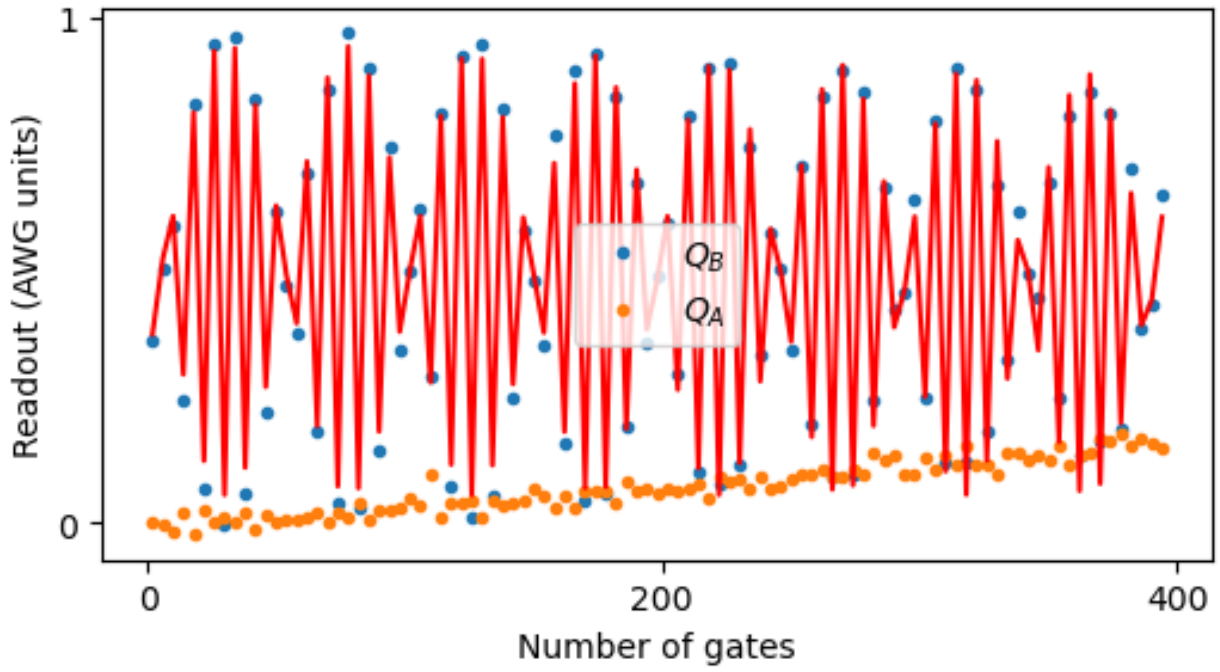

Figure 7.9: **Calibration data for ϕ_{10} and ϕ_D measurement.** Performing a blue sideband drive at the desired frequency while sweeping the amplitude of a cancellation pulse.

yielding

$$
\begin{aligned}
H'' = U_2^\dagger H' U_2 = &-\frac{\omega_a - \omega_d + \delta\omega_a}{2}\sigma_{za} - \frac{\omega_b - \omega_d + \delta\omega_b}{2}\sigma_{zb} \\
&+ J_{\mathrm{ac}}\cos(\omega_d t)\left(\cos(\omega_d t)\left[\cos\left(\frac{\alpha E_{La}\langle\phi_a\rangle_{01}}{\omega_a - \omega_d}\right)\sigma_{xa} - \sin\left(\frac{\alpha E_{La}\langle\phi_a\rangle_{01}}{\omega_a - \omega_d}\right)\sigma_{za}\right] + \sin(\omega_d t)\sigma_{ya}\right) \\
&\times\left(\cos(\omega_d t)\left[\cos\left(\frac{\beta E_{Lb}\langle\phi_b\rangle_{01}}{\omega_b - \omega_d}\right)\sigma_{xb} - \sin\left(\frac{\beta E_{Lb}\langle\phi_b\rangle_{01}}{\omega_b - \omega_d}\right)\sigma_{zb}\right] + \sin(\omega_d t)\sigma_{yb}\right),
\end{aligned}
$$

where e.g. $\delta\omega_a = \frac{(\alpha E_{La}\langle\phi_a\rangle_{01})^2/2}{\omega_a - \omega_d}$. Rotating back into the lab frame and including only the leading-order corrections in the two-qubit drive term, we obtain

$$
\begin{aligned}
H''' = &-\frac{\omega_a + \delta\omega_a}{2}\sigma_{za} - \frac{\omega_b + \delta\omega_b}{2}\sigma_{zb} \\
&+ J_{\mathrm{ac}}\cos(\omega_d t)\left(\sigma_{xa} - \frac{\alpha E_{La}\langle\phi_a\rangle_{01}}{\omega_a - \omega_d}\sigma_{za}\right) \\
&\times\left(\sigma_{xb} - \frac{\beta E_{Lb}\langle\phi_b\rangle_{01}}{\omega_b - \omega_d}\sigma_{zb}\right).
\end{aligned}
\tag{7.8}
$$

Thus the leading-order effects of ac-flux crosstalk are to renormalize the qubit frequencies as well as modify the effective two-qubit drive term from XX to a combination of XX, ZX, XZ and ZZ.

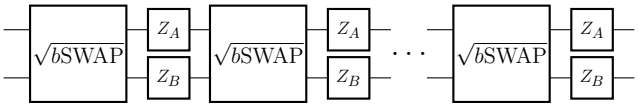

Figure 7.10: **Gate sequence for the first step of phase calibration**

The DC and RF flux crosstalk of the system both have significant impact on the device behavior and require proper calibration. We measure the DC flux crosstalk by performing 2D flux sweeps for different flux channels, and measure how certain flux dependent features change with both fluxes. The slope of this line is the DC flux crosstalk of our system.

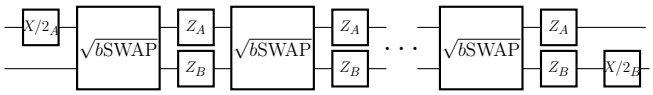

Figure 7.11: **Gate sequence for the second step of phase calibration**

For RF flux crosstalk, we simultaneously send two compensation pulses with the original drive pulse to the three RF flux lines. Each compensation pulse has the same length as the original, and we modify their phase and amplitude for maximum flux crosstalk cancellation. Since the phases of the two compensation pulses are independent of all other parameters, we calibrate them individually first. We play a drive pulse and a compensation pulse at the blue sideband frequency, with the compensation pulse amplitude smaller than the complete cancellation amplitude, and perform a Rabi experiment. Since the flux crosstalk is an off resonant drive to a qubit, it will change the qubit frequency due to AC Stark shift. The Rabi contrast will be at its maximum when the qubit frequency shift is at its minimum, due to the drive frequency being the sum of bare qubit frequencies. We search for the maximum contrast point while performing the blue sideband rotation (shown in fig 7.3), and determine the correct phase for the compensation pulses.

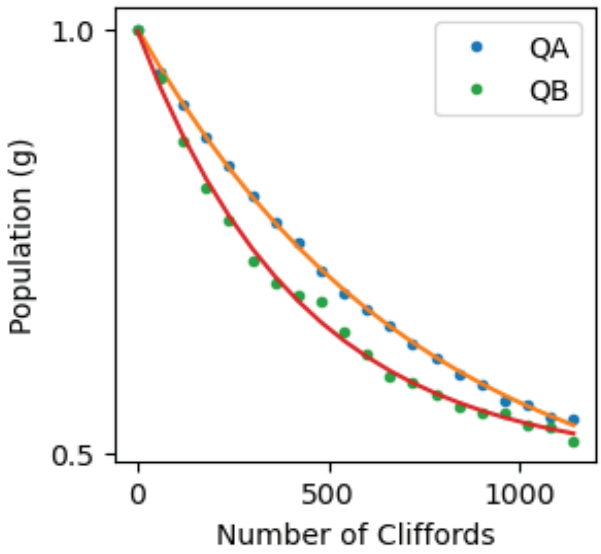

Figure 7.12: **Simultaneous single qubit randomized benchmarking for both qubits.** Qubit A single qubit gate fidelity is 99.93%, Qubit B single qubit gate fidelity is 99.89%.

After we have the correct phases for both compensation channels, we sweep the amplitude of the compensation pulses to find the optimal cancellation amplitude. Similar to the phase calibration process above, we search for the cancellation amplitude where the blue sideband oscillation is at its maximum contrast (Shown in fig 7.4). Since the cancellation gains from the two qubit channels will affect each other, we did this iteratively to find the optimal amplitudes for both of them.

Due to the linear nature of the flux crosstalk, the amplitude of drive pulse and compensation pulses have a linear relationship, and the phase difference between all three pulses is always the same. With cancellation phases and amplitudes for one drive pulse calibrated, we can utilize this rule to derive compensation pulses for all blue sideband drive pulses. The two qubit gates reported in this manuscript are all constructed in this way, with the coupler drive pulse and cancellation pulses on each qubit.

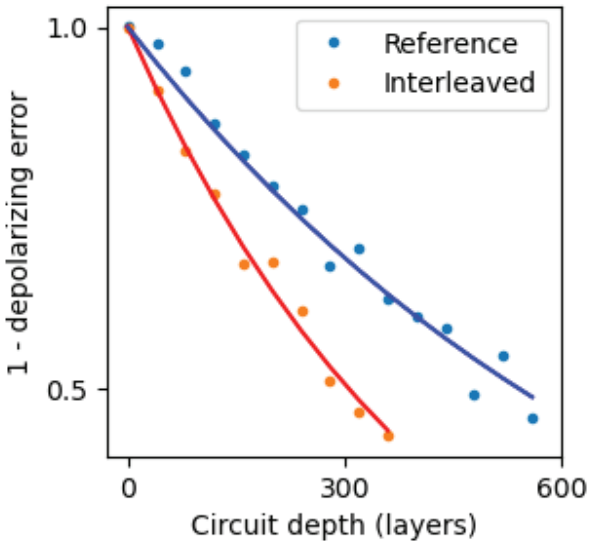

Figure 7.13: **Cross entropy benchmarking data** with Reference sequence fidellity 99.88%, and interleaved trace fidelity 99.78%. This give us a two qubit gate fidelity 99.91%.

7.3 Gate calibrations

The system is controlled with flux modulation instead of charge drive, thus there are no charge drive lines. We have described the flux cancellation procedures above, and with the cancellation pulses calibrated, we can start the calibration of single and two qubit gates.

For the single qubit gates, we flux modulate the qubits at their corresponding frequencies. Since the phase matrix element $\langle 0|\phi|1\rangle$ is significantly larger than the charge one $\langle 0|n|1\rangle$, we can realize very fast single qubit gates with much less power. With qubit frequencies at 48 and 61MHz, the single qubit gates in this experiment are Gaussian pulses with length 83.3 and 65.1ns, only around 4 qubit Larmor cycles. At this gate length, the Bloch-Siegert shift is only around several kHz, and its contribution to the gate error is insignificant. The Gaussian gates' fidelities are measured through simultaneous randomized benchmarking, their gate fidelities are 99.79% for qubit A and 99.88% for qubit B. We further optimized the single qubit gates with DRAG pulses, and improved single qubit gate fidelities to 99.93%. Master equation simulation gives a decoherence error of 6×10^{-4} with our gate length, thus it is the only limiting factor for our single qubit gates.

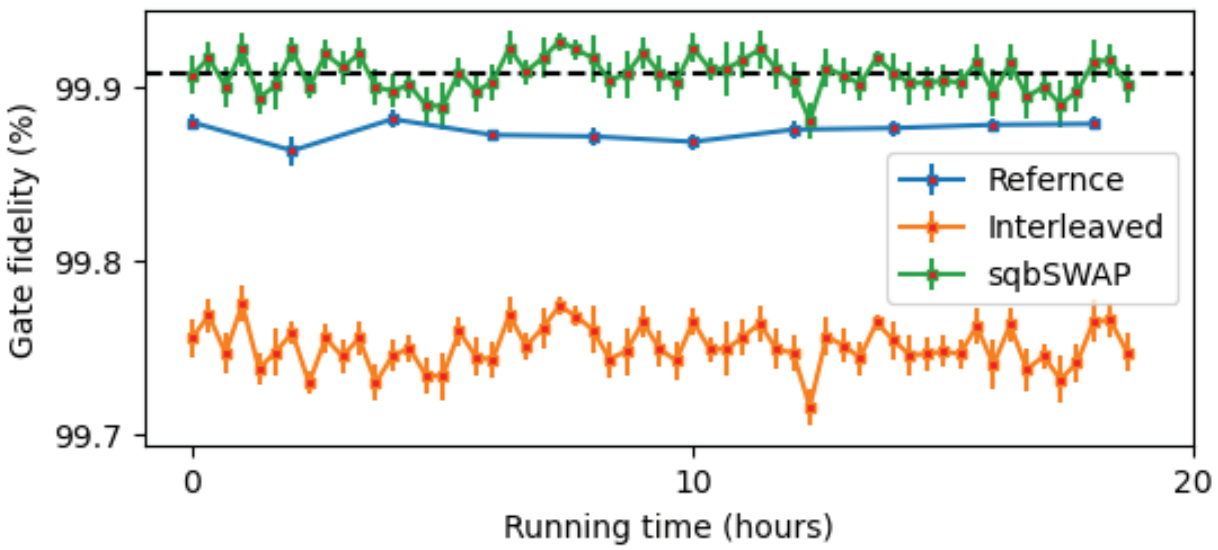

Figure 7.14: **20 hour long consecutive cross entropy benchmarking runs for $\sqrt{b\text{SWAP}}$ gates,** showing an average gate fidelity 99.91%.

The parametric driven two qubit gate consists of a flux modulation pulse on the coupler, and two single qubit Z gates for phase corrections. RF cancellation pulses are implemented for the coupler flux drive, which realizes sideband transitions between $|ge\rangle$ and $|eg\rangle$ (red sideband), and $|gg\rangle$ and $|ee\rangle$ (blue sideband). The red and blue sideband frequencies are 13.3 and 110.2MHz respectively, and the $\sqrt{i\text{SWAP}}$ gate length is 250ns, while a $\sqrt{b\text{SWAP}}$ takes only 100ns. Due to the very low frequencies of these pulses, they only have 3 and 11 oscillation periods respectively, but the effect of counter rotating terms is still negligible in both cases.

The parametric drive can generate any entangled states up to an arbitrary phase. We measure the phases of the parametric drive with specifically designed sequences, and cancel the extra phases with single qubit Z gates and an extra phase on the drive pulse. These calibration sequences were designed to amplify the gate errors. The gate calibration process consists of two steps, the rotation angle calibration and phase calibrations. We can write the Hermitian matrix for a gate generated by a parametric drive on the coupler as

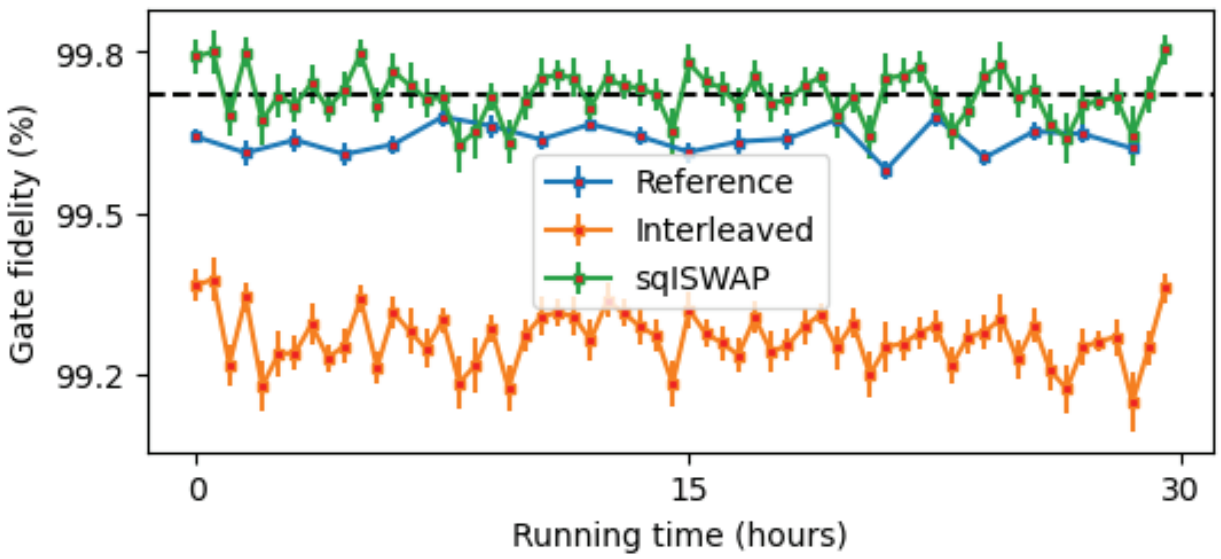

Figure 7.15: **30 hour long consecutive cross entropy benchmarking runs for $\sqrt{i\text{SWAP}}$ gates,** showing an average gate fidelity 99.72%.

$$\begin{pmatrix} \cos\theta & 0 & 0 & ie^{i\phi_D}\sin\theta \\ 0 & e^{i\phi_{01}} & 0 & 0 \\ 0 & 0 & e^{i\phi_{10}} & 0 \\ ie^{i(\phi_{11}-\phi_D)}\sin\theta & 0 & 0 & e^{i\phi_{11}}\cos\theta \end{pmatrix}$$

for blue sideband rotations and

$$\begin{pmatrix} 1 & 0 & 0 & 0 \\ 0 & e^{i\phi_{01}}\cos\theta & ie^{i(\phi_{01}+\phi_D)}\sin\theta & 0 \\ 0 & ie^{i(\phi_{10}-\phi_D)}\sin\theta & e^{i\phi_{10}}\cos\theta & 0 \\ 0 & 0 & 0 & e^{i\phi_{11}} \end{pmatrix}$$

for red sideband rotations, where ϕ_D is the phase of the coupler drive, ϕ_{01}, ϕ_{10}, and ϕ_{11} are phases due to the frequency shift of levels while the drive is on, which have relationship $\phi_{11} = \phi_{01} + \phi_{10} + \phi_{zz}$. In our system, since all frequency shifts and the ZZ term during the parametric drive are small, we have $\phi_{11} \approx \phi_{01} + \phi_{10}$ and ϕ_{11} close to 0. We first calibrate the rotation angle (θ). We fixed the pulse length for red sideband at $99000/384 \approx 257.8$ns and blue sideband at $39000/384 \approx 101.6$ns. Since our AWG (Xilinx RFsoc) has a 384MHz processor, the pulse lengths are integer numbers of 1000/384ns. We initialize the system in

state $|00\rangle$, sweep the pulse amplitude while playing the same pulse consecutively for $4n+2$ times, and look for the amplitude that gives us the highest fidelity $|11\rangle$ state. With playing the same gate for up to 402 times, we can obtain the value of parameter θ up to 1×10^{-4} in precision.

With θ calibrated to be $\pi/4$, gate phases $\phi_{01}, \phi_{10}, \phi_{11}$ and ϕ_D are subsequently calibrated. Since the calibration process is very similar for $\sqrt{i\text{SWAP}}$ and $\sqrt{b\text{SWAP}}$ gates, here we only use $\sqrt{b\text{SWAP}}$ as an example for explanation. We calibrate these phases with sequence shown in Fig. 7.10, where Z_A and Z_B are single qubit phase gates on each qubit with phase ϕ_A and ϕ_B. A unit consists of one $\sqrt{b\text{SWAP}}$ gate and two single qubit Z gates, and we noticed that with $4n+2$ number of units, only when $\phi_A + \phi_B = -\phi_{11}$ do we get a bSWAP gate up to some phases. Thus we play a sequence of 321 units while sweeping ϕ_A (shown in fig 7.8), and measured ϕ_{11} to be around -3 degrees. We subsequently play the sequence shown in Fig. 7.11, and with $4n+2$ units, we have qubit B ground state population,

$$\frac{1}{2}(1 + (-1)^n \sin(4n(\phi_{10} - \phi_{11}) + 2(\phi_{10} - \phi_{11}) + \phi_D)) \tag{7.9}$$

and qubit A ground state population should always be 0 for all the n values. Fitting this function gives us $\phi_{10} - \phi_{11}$ and $2\phi_{10} - 2\phi_{11} + \phi_D$ (shown in figure 7.9). With the ϕ_{11} value measured from the step above, we can derive ϕ_{10}, ϕ_{11}, and ϕ_D. Since ϕ_{ZZ} is very small in our system, we can calculate ϕ_{01} as $\phi_{11} - \phi_{10}$, and the result is very close to directly measuring ϕ_{01} by switching operations on qubit A and qubit B.

After the calibration, we set qubit A Z gate after the parametric coupler drive $\phi_A = -\phi_{10}$, qubit B Z gate $\phi_B = -\phi_{01}$, and change the drive phase by $-\phi_D$. In this experiment all the single qubit Z gates are virtual, therefore we only need to update the phase of the pulses after a $\sqrt{b\text{SWAP}}$ or $\sqrt{i\text{SWAP}}$ gate for each qubit.

With the calibrations and phase corrections, we get $\sqrt{i\text{SWAP}}$ and $\sqrt{b\text{SWAP}}$ gates

$$\begin{pmatrix} 1 & 0 & 0 & 0 \\ 0 & 1/\sqrt{2} & i/\sqrt{2} & 0 \\ 0 & i/\sqrt{2} & 1/\sqrt{2} & 0 \\ 0 & 0 & 0 & 1 \end{pmatrix} \begin{pmatrix} 1/\sqrt{2} & 0 & 0 & i/\sqrt{2} \\ 0 & 1 & 0 & 0 \\ 0 & 0 & 1 & 0 \\ i/\sqrt{2} & 0 & 0 & 1/\sqrt{2} \end{pmatrix}$$

We performed state tomographies on the Bell states created by these gates (see Fig. 7.6), and also had process tomography to verify the unitary matrix elements (see Fig. 7.7). In order to precisely benchmark the fidelities of the two qubit gates, we implemented Cross Entropy Benchmarking. We first measure the depolarizing error of reference gate sequences, which are made of single qubit $\pi/2$ gates with random phases. We subsequently interleave the $\sqrt{i\text{SWAP}}$ or $\sqrt{b\text{SWAP}}$ gates between each pair of single qubit gates, and measure the depolarizing error of the entire interleaved sequence. The gate fidelity can be calculated with the depolarizing errors as

$$F = p + (1 - p)/D \tag{7.10}$$

where p is the depolarizing error of the two qubit gate, and F is the derived gate fidelity. To measure the $\sqrt{i\text{SWAP}}$ gate fidelity, we interleaved it in reference sequences consisting of Gaussian single qubit gates. We measured reference depolarizing error $\sim 3.2\times10^{-3}$ and total depolarizing error $\sim 6 \times 10^{-3}$. With equation 7.10 we derive the $\sqrt{i\text{SWAP}}$ fidelity 99.72%. For $\sqrt{b\text{SWAP}}$ gates, we implemented the DRAG single qubit gates for improved reference sequence fidelity. We measured depolarizing error $\sim 1.3 \times 10^{-3}$ with DRAG pulses and total depolarizing error $\sim 2.4 \times 10^{-3}$ with interleaved sequences, which gives a $\sqrt{b\text{SWAP}}$ fidelity 99.91%. Finally we constructed a CNOT gate with two $\sqrt{b\text{SWAP}}$ gates and five single qubit gates, and measured the CNOT fidelity to be 99.5% with two qubit Randomized Benchmarking.

CHAPTER 8

CONCLUSION AND OUTLOOK

We have presented the low-frequency (heavy) fluxonium qubits, which operate in a special regime unexplored with previous superconducting circuits. We demonstrated that these qubits have great coherences due to their low frequencies, and we achieved a factor of 5 - 10 increased compared to the transmon qubits made in our lab. We were also able to initialize the qubits simply by performing readout and active feedback before each experiment, and achieved 95% initialization fidelity. We demonstrated fast, high-fidelity single and two qubit gates for the heavy fluxonium qubits, and achieved 99.93% fidelity for single qubit gates and 99.91% fidelity for two qubit gates.

Due to the large anharmonicity of the fluxonium qubits, the computational levels only have a frequency splitting of tens of MHz, while the next level is around several GHz. This has brought very unique properties to the heavy fluxonium qubits. For example, with our single and two qubit gate design, the gate error due to leakage is always negligible. This provides great freedom in quantum control, since we can shape the pulse almost arbitrarily without worrying about any excitation to the other levels. This feature is also useful in the implementation of quantum error correction, and can simplify the control of large scale quantum processors since none of the higher levels has to be put under consideration.

All control pulses used in performing single and two qubit gate operations are flux pulses with very low frequencies. Due to the design of the two qubit device, there is large crosstalk between the flux control lines, and needs to be compensated with flux cancellation pulses. However, there are many ways to significantly reduce the flux crosstalk between superconducting loops, including significantly increasing the coupling between the flux line and its corresponding loop, or utilizing 3D integration to reduce the flux crosstalk. The level of RF flux crosstalk can be reduced to 1×10^{-3} to 1×10^{-2} if it is well engineered, and the effect of such crosstalk will be much less than the typical charge crosstalk seen in charge driven

and charge coupled devices.

The natural next step for fluxonium qubits is to scale up. The tunable coupler design demonstrated in this thesis can be intuitively scaled to a 1D chain of fluxonium qubits, with a tunable coupler between each pair of them. However, 2D expansion of this design will generate additional loops on top of the existing ones, and this could make the operation of such quantum processors much more complicated. The two qubit gate protocol realized with this tunable coupler design does not involve any higher levels, therefore has significant advantages in a large scale quantum processor. The next step of exploring the fluxonium control options could be looking for a parametricly driven gate that can be realized with tunable couplers more friendly for scaling up.

REFERENCES

[1] Suppressing quantum errors by scaling a surface code logical qubit. *Nature*, 614(7949): 676–681, 2023.

[2] A. A. Abdumalikov Jr, O Astafiev, Alexandre M Zagoskin, Yu A Pashkin, Y Nakamura, and J. S. Tsai. Electromagnetically induced transparency on a single artificial atom. *Physical Review Letters*, 104(19):193601, 2010.

[3] E. Arimondo. V Coherent Population Trapping in Laser Spectroscopy. *Progress in Optics*, 35:257–354, 1996.

[4] Frank Arute, Kunal Arya, Ryan Babbush, Dave Bacon, Joseph C Bardin, Rami Barends, Rupak Biswas, Sergio Boixo, Fernando GSL Brandao, David A Buell, et al. Quantum supremacy using a programmable superconducting processor. *Nature*, 574 (7779):505–510, 2019.

[5] R Barends, L Lamata, J Kelly, L García-Álvarez, AG Fowler, A Megrant, E Jeffrey, TC White, D Sank, JY Mutus, et al. Digital quantum simulation of fermionic models with a superconducting circuit. *Nature Communications*, 6, 2015.

[6] Rami Barends, Julian Kelly, Anthony Megrant, Daniel Sank, Evan Jeffrey, Yu Chen, Yi Yin, Ben Chiaro, Josh Mutus, Charles Neill, et al. Coherent Josephson qubit suitable for scalable quantum integrated circuits. *Physical Review Letters*, 111(8): 080502, 2013.

[7] Rami Barends, Julian Kelly, Anthony Megrant, Andrzej Veitia, Daniel Sank, Evan Jeffrey, Ted C White, Josh Mutus, Austin G Fowler, Brooks Campbell, et al. Superconducting quantum circuits at the surface code threshold for fault tolerance. *Nature*, 508(7497):500–503, 2014.

[8] Matthew T Bell, Joshua Paramanandam, Lev B Ioffe, and Michael E Gershenson. Protected Josephson rhombus chains. *Physical Review Letters*, 112(16):167001, 2014.

[9] D. M. Berns, W. D. Oliver, S. O. Valenzuela, A. V. Shytov, K. K. Berggren, L. S. Levitov, and T. P. Orlando. Coherent quasiclassical dynamics of a persistent current qubit. *Phys. Rev. Lett.*, 97:150502, Oct 2006. doi:10.1103/PhysRevLett.97.150502. URL `https://link.aps.org/doi/10.1103/PhysRevLett.97.150502`.

[10] Lev S. Bishop, J. M. Chow, Jens Koch, A.A. Houck, M.H Devoret, E. Thuneberg, S.M. Girvin, and R.J. Schoelkopf. Nonlinear response of the vacuum rabi resonance. *Nature Physics*, 5:105–109, 2009.

[11] Alexandre Blais, Jay Gambetta, A. Wallraff, D. I. Schuster, S. M. Girvin, M. H. Devoret, and R. J. Schoelkopf. Quantum-information processing with circuit quantum electrodynamics. *Phys. Rev. A*, 75:032329, Mar 2007. doi:10.1103/PhysRevA.75.032329. URL `https://link.aps.org/doi/10.1103/PhysRevA.75.032329`.

[12] Heinz-Peter Breuer and Francesco Petruccione. *The theory of open quantum systems*. Oxford University Press on Demand, 2002.

[13] Daniel L. Campbell, Yun-Pil Shim, Bharath Kannan, Roni Winik, Alexander Melville, Bethany M. Niedzielski, Jonilyn L. Yoder, Charles Tahan, Simon Gustavsson, and William D. Oliver. Universal non-adiabatic control of small-gap superconducting qubits, 2020.

[14] Gianluigi Catelani, Jens Koch, Luigi Frunzio, RJ Schoelkopf, Michel H Devoret, and LI Glazman. Quasiparticle relaxation of superconducting qubits in the presence of flux. *Physical Review Letters*, 106(7):077002, 2011.

[15] Josephine B Chang, Michael R Vissers, Antonio D Córcoles, Martin Sandberg, Jiansong Gao, David W Abraham, Jerry M Chow, Jay M Gambetta, Mary Beth Rothwell, George A Keefe, et al. Improved superconducting qubit coherence using titanium nitride. *Applied Physics Letters*, 103(1):012602, 2013.

[16] I Chiorescu, Y Nakamura, CJP Ma Harmans, and JE Mooij. Coherent quantum dynamics of a superconducting flux qubit. *Science*, 299(5614):1869–1871, 2003.

[17] I Chiorescu, P Bertet, K Semba, Y Nakamura, CJPM Harmans, and JE Mooij. Coherent dynamics of a flux qubit coupled to a harmonic oscillator. *Nature*, 431(7005): 159–162, 2004.

[18] J. M. Chow, J. M. Gambetta, L. Tornberg, Jens Koch, Lev S. Bishop, A. A. Houck, B. R. Johnson, L. Frunzio, S. M. Girvin, and R. J. Schoelkopf. Randomized benchmarking and process tomography for gate errors in a solid-state qubit. *Phys. Rev. Lett.*, 102:090502, Mar 2009. doi:10.1103/PhysRevLett.102.090502. URL `https://link.aps.org/doi/10.1103/PhysRevLett.102.090502`.

[19] Jerry M Chow, Jay M Gambetta, Easwar Magesan, David W Abraham, Andrew W Cross, BR Johnson, Nicholas A Masluk, Colm A Ryan, John A Smolin, Srikanth J Srinivasan, et al. Implementing a strand of a scalable fault-tolerant quantum computing fabric. *Nat. Comm.*, 5, 2014.

[20] Aashish A Clerk, Michel H Devoret, Steven M Girvin, Florian Marquardt, and Robert J Schoelkopf. Introduction to quantum noise, measurement, and amplification. *Reviews of Modern Physics*, 82(2):1155, 2010.

[21] Claude Cohen-Tannoudji and Alfred Kastler. I optical pumping. *Progress in optics*, 5: 1–81, 1966.

[22] B.J. Dalton, R. McDuff, and P.L. Knight. Coherent Population Trapping. *Optica Acta: International Journal of Optics*, 32(1):61–70, 1 1985. doi:10.1080/713821645. URL `http://www.tandfonline.com/doi/abs/10.1080/713821645`.

[23] S Debnath, NM Linke, C Figgatt, KA Landsman, K Wright, and C Monroe. Demonstration of a small programmable quantum computer with atomic qubits. *Nature*, 536 (7614):63–66, 2016.

[24] Joshua M Dempster, Bo Fu, David G Ferguson, David I Schuster, and Jens Koch. Understanding degenerate ground states of a protected quantum circuit in the presence of disorder. *Physical Review B*, 90(9):094518, 2014.

[25] Michel H Devoret and Robert J Schoelkopf. Superconducting circuits for quantum information: an outlook. *Science*, 339(6124):1169–1174, 2013.

[26] L DiCarlo, JM Chow, JM Gambetta, Lev S Bishop, BR Johnson, DI Schuster, J Majer, A Blais, L Frunzio, SM Girvin, et al. Demonstration of two-qubit algorithms with a superconducting quantum processor. *Nature*, 460(7252):240–244, 2009.

[27] A Dunsworth, A Megrant, C Quintana, Zijun Chen, R Barends, B Burkett, B Foxen, Yu Chen, B Chiaro, A Fowler, et al. Characterization and reduction of capacitive loss induced by sub-micron Josephson junction fabrication in superconducting qubits. *Applied Physics Letters*, 111(2):022601, 2017.

[28] N. Earnest, S. Chakram, Y. Lu, N. Irons, R. K. Naik, N. Leung, L. Ocola, D. A. Czaplewski, B. Baker, Jay Lawrence, Jens Koch, and D. I. Schuster. Realization of a Λ system with metastable states of a capacitively shunted fluxonium. *Phys. Rev. Lett.*, 120:150504, Apr 2018. doi:10.1103/PhysRevLett.120.150504. URL `https://link.aps.org/doi/10.1103/PhysRevLett.120.150504`.

[29] A Fedorov, AK Feofanov, P Macha, P Forn-Díaz, CJPM Harmans, and JE Mooij. Strong coupling of a quantum oscillator to a flux qubit at its symmetry point. *Physical Review Letters*, 105(6):060503, 2010.

[30] Austin G. Fowler, Matteo Mariantoni, John M. Martinis, and Andrew N. Cleland. Surface codes: Towards practical large-scale quantum computation. *Phys. Rev. A*, 86: 032324, Sep 2012. doi:10.1103/PhysRevA.86.032324. URL `https://link.aps.org/doi/10.1103/PhysRevA.86.032324`.

[31] Austin G Fowler, Matteo Mariantoni, John M Martinis, and Andrew N Cleland. Surface codes: Towards practical large-scale quantum computation. *Physical Review A*, 86(3):032324, 2012.

[32] Jay M Gambetta, Conal E Murray, Y-K-K Fung, Douglas T McClure, Oliver Dial, William Shanks, Jeffrey W Sleight, and Matthias Steffen. Investigating surface loss effects in superconducting transmon qubits. *IEEE Transactions on Applied Superconductivity*, 27(1):1–5, 2016.

[33] Peter Groszkowski and Jens Koch. Scqubits: a python package for superconducting qubits. *Quantum*, 5:583, Nov 2021. ISSN 2521-327X. doi:10.22331/q-2021-11-17-583. arXiv:2107.08552 [quant-ph].

[34] Peter Groszkowski, A Di Paolo, A L Grimsmo, A Blais, D I Schuster, A A Houck, and Jens Koch. Coherence properties of the 0-π qubit. *New Journal of Physics*, 20(4): 043053, apr 2018. doi:10.1088/1367-2630/aab7cd. URL https://doi.org/10.1088%2F1367-2630%2Faab7cd.

[35] M. Hatridge, S. Shankar, M. Mirrahimi, F. Schackert, K. Geerlings, T. Brecht, K. M. Sliwa, B. Abdo, L. Frunzio, S. M. Girvin, R. J. Schoelkopf, and M. H. Devoret. Quantum back-action of an individual variable-strength measurement. *Science*, 339(6116):178–181, 2013. ISSN 0036-8075. doi:10.1126/science.1226897. URL https://science.sciencemag.org/content/339/6116/178.

[36] TM Hazard, Andras Gyenis, Agustin Di Paolo, AT Asfaw, Stephen Aplin Lyon, AAHA Blais, and Andrew Addison Houck. Nanowire superinductance fluxonium qubit. *Physical review letters*, 122(1):010504, 2019.

[37] C. Hicke, L. F. Santos, and M. I. Dykman. Fault-tolerant landau-zener quantum gates. *Phys. Rev. A*, 73:012342, Jan 2006. doi:10.1103/PhysRevA.73.012342. URL https://link.aps.org/doi/10.1103/PhysRevA.73.012342.

[38] AA Houck, JA Schreier, BR Johnson, JM Chow, Jens Koch, JM Gambetta, DI Schuster, L Frunzio, MH Devoret, SM Girvin, et al. Controlling the spontaneous emission of a superconducting transmon qubit. *Physical Review Letters*, 101(8):080502, 2008.

[39] G. Ithier, E. Collin, P. Joyez, P. J. Meeson, D. Vion, D. Esteve, F. Chiarello, A. Shnirman, Y. Makhlin, J. Schriefl, and G. Schön. Decoherence in a superconducting quantum bit circuit. *Phys. Rev. B*, 72:134519, Oct 2005. doi:10.1103/PhysRevB.72.134519. URL https://link.aps.org/doi/10.1103/PhysRevB.72.134519.

[40] XY Jin, A Kamal, AP Sears, T Gudmundsen, D Hover, J Miloshi, R Slattery, F Yan, J Yoder, TP Orlando, et al. Thermal and residual excited-state population in a 3d transmon qubit. *Physical Review Letters*, 114(24):240501, 2015.

[41] J.R. Johansson, P.D. Nation, and Franco Nori. Qutip 2: A python framework for the dynamics of open quantum systems. *Computer Physics Communications*, 184(4):1234 – 1240, 2013. ISSN 0010-4655. doi:https://doi.org/10.1016/j.cpc.2012.11.019. URL http://www.sciencedirect.com/science/article/pii/S0010465512003955.

[42] BR Johnson, MD Reed, AA Houck, DI Schuster, Lev S Bishop, E Ginossar, JM Gambetta, L DiCarlo, L Frunzio, SM Girvin, et al. Quantum non-demolition detection of single microwave photons in a circuit. *Nature Physics*, 6(9):663–667, 2010.

[43] Abhinav Kandala, Antonio Mezzacapo, Kristan Temme, Maika Takita, Markus Brink, Jerry M Chow, and Jay M Gambetta. Hardware-efficient variational quantum eigensolver for small molecules and quantum magnets. *Nature*, 549(7671):242–246, 2017.

[44] Julian Kelly, R Barends, AG Fowler, A Megrant, E Jeffrey, TC White, D Sank, JY Mutus, B Campbell, Yu Chen, et al. State preservation by repetitive error detection in a superconducting quantum circuit. *Nature*, 519(7541):66–69, 2015.

[45] William R Kelly, Zachary Dutton, John Schlafer, Bhaskar Mookerji, Thomas A Ohki, Jeffrey S Kline, and David P Pappas. Direct observation of coherent population trapping in a superconducting artificial atom. *Physical Review Letters*, 104(16):163601, 2010.

[46] Youngseok Kim, Andrew Eddins, Sajant Anand, Ken Xuan Wei, Ewout Van Den Berg, Sami Rosenblatt, Hasan Nayfeh, Yantao Wu, Michael Zaletel, Kristan Temme, et al. Evidence for the utility of quantum computing before fault tolerance. *Nature*, 618 (7965):500–505, 2023.

[47] Emanuel Knill, Dietrich Leibfried, Rolf Reichle, Joe Britton, R Brad Blakestad, John D Jost, Chris Langer, Roee Ozeri, Signe Seidelin, and David J Wineland. Randomized benchmarking of quantum gates. *Physical Review A*, 77(1):012307, 2008.

[48] Jens Koch, Terri M. Yu, Jay Gambetta, A. A. Houck, D. I. Schuster, J. Majer, Alexandre Blais, M. H. Devoret, S. M. Girvin, and R. J. Schoelkopf. Charge-insensitive qubit design derived from the Cooper pair box. *Physical Review A*, 76:042319, Oct 2007. doi:10.1103/PhysRevA.76.042319.

[49] Jens Koch, V Manucharyan, MH Devoret, and LI Glazman. Charging effects in the inductively shunted Josephson junction. *Physical Review Letters*, 103(21):217004, 2009.

[50] A Kou, WC Smith, U Vool, RT Brierley, H Meier, L Frunzio, SM Girvin, LI Glazman, and MH Devoret. Fluxonium-based artificial molecule with a tunable magnetic moment. *Physical Review X*, 7(3):031037, 2017.

[51] Philip Krantz, Morten Kjaergaard, Fei Yan, Terry P Orlando, Simon Gustavsson, and William D Oliver. A quantum engineer's guide to superconducting qubits. *Applied Physics Reviews*, 6(2):021318, 2019.

[52] Florent Lecocq, Ioan M Pop, Zhihui Peng, Iulian Matei, Thierry Crozes, Thierry Fournier, Cécile Naud, Wiebke Guichard, and Olivier Buisson. Junction fabrication by shadow evaporation without a suspended bridge. *Nanotechnology*, 22(31):315302, 2011.

[53] Yen-Hsiang Lin, Long B Nguyen, Nicholas Grabon, Jonathan San Miguel, Natalia Pankratova, and Vladimir E Manucharyan. Demonstration of protection of a superconducting qubit from energy decay. *Physical review letters*, 120(15):150503, 2018.

[54] Yao Lu, Srivatsan Chakram, Nelson Leung, Nathan Earnest, Ravi K Naik, Ziwen Huang, Peter Groszkowski, Eliot Kapit, Jens Koch, and David I Schuster. Universal stabilization of a parametrically coupled qubit. *Physical Review Letters*, 119(15): 150502, 2017.

[55] Easwar Magesan, Jay M. Gambetta, B. R. Johnson, Colm A. Ryan, Jerry M. Chow, Seth T. Merkel, Marcus P. da Silva, George A. Keefe, Mary B. Rothwell, Thomas A. Ohki, Mark B. Ketchen, and M. Steffen. Efficient measurement of quantum gate error

by interleaved randomized benchmarking. *Phys. Rev. Lett.*, 109:080505, Aug 2012. doi:10.1103/PhysRevLett.109.080505. URL `https://link.aps.org/doi/10.1103/PhysRevLett.109.080505`.

[56] P. Magnard, P. Kurpiers, B. Royer, T. Walter, J.-C. Besse, S. Gasparinetti, M. Pechal, J. Heinsoo, S. Storz, A. Blais, and A. Wallraff. Fast and unconditional all-microwave reset of a superconducting qubit. *Phys. Rev. Lett.*, 121:060502, Aug 2018. doi:10.1103/PhysRevLett.121.060502. URL `https://link.aps.org/doi/10.1103/PhysRevLett.121.060502`.

[57] Vladimir E. Manucharyan, Jens Koch, Markus Brink, Leonid I. Glazman, and Michel H. Devoret. Coherent oscillations between classically separable quantum states of a superconducting loop, 2009.

[58] Vladimir E Manucharyan, Jens Koch, Leonid I Glazman, and Michel H Devoret. Fluxonium: Single Cooper-pair circuit free of charge offsets. *Science*, 326(5949):113–116, 2009.

[59] Vladimir E Manucharyan, Nicholas A Masluk, Archana Kamal, Jens Koch, Leonid I Glazman, and Michel H Devoret. Evidence for coherent quantum phase slips across a Josephson junction array. *Physical Review B*, 85(2):024521, 2012.

[60] John M Martinis and A Megrant. Ucsb final report for the csq program: Review of decoherence and materials physics for superconducting qubits. *arXiv preprint arXiv:1410.5793*, 2014.

[61] John M Martinis, Michel H Devoret, and John Clarke. Experimental tests for the quantum behavior of a macroscopic degree of freedom: The phase difference across a Josephson junction. *Physical Review B*, 35(10):4682, 1987.

[62] Michael Metcalfe, E Boaknin, V Manucharyan, R Vijay, I Siddiqi, C Rigetti, L Frunzio, RJ Schoelkopf, and MH Devoret. Measuring the decoherence of a quantronium qubit with the cavity bifurcation amplifier. *Physical Review B*, 76(17):174516, 2007.

[63] Chris Monroe, D. M. Meekhof, B. E. King, Wayne M Itano, and David J Wineland. Demonstration of a fundamental quantum logic gate. *Physical Review Letters*, 75(25): 4714, 1995.

[64] JE Mooij, TP Orlando, L Levitov, Lin Tian, Caspar H Van der Wal, and Seth Lloyd. Josephson persistent-current qubit. *Science*, 285(5430):1036–1039, 1999.

[65] Yu Nakamura, Yu A Pashkin, and Jaw Shen Tsai. Coherent control of macroscopic quantum states in a single-Cooper-pair box. *nature*, 398(6730):786–788, 1999.

[66] Ani Nersisyan, Stefano Poletto, Nasser Alidoust, Riccardo Manenti, Russ Renzas, Cat-Vu Bui, Kim Vu, Tyler Whyland, Yuvraj Mohan, Eyob A Sete, et al. Manufacturing low dissipation superconducting quantum processors. *arXiv preprint arXiv:1901.08042*, 2019.

[67] Konstantin N. Nesterov, Ivan V. Pechenezhskiy, Chen Wang, Vladimir E. Manucharyan, and Maxim G. Vavilov. Microwave-activated controlled-z gate for fixed-frequency fluxonium qubits. *Phys. Rev. A*, 98:030301(R), Sep 2018. doi:10.1103/PhysRevA.98.030301. URL `https://link.aps.org/doi/10.1103/PhysRevA.98.030301`.

[68] W Neuhauser, M Hohenstatt, P. E. Toschek, and H Dehmelt. Localized visible ba+ mono-ion oscillator. *Physical Review A*, 22(3):1137, 1980.

[69] Long B. Nguyen, Yen-Hsiang Lin, Aaron Somoroff, Raymond Mencia, Nicholas Grabon, and Vladimir E. Manucharyan. High-coherence fluxonium qubit. *Phys. Rev. X*, 9:041041, Nov 2019. doi:10.1103/PhysRevX.9.041041. URL `https://link.aps.org/doi/10.1103/PhysRevX.9.041041`.

[70] TL Nicholson, SL Campbell, RB Hutson, GE Marti, BJ Bloom, RL McNally, Wei Zhang, MD Barrett, MS Safronova, GF Strouse, et al. Systematic evaluation of an atomic clock at 2 [times] 10-18 total uncertainty. *Nature communications*, 6, 2015.

[71] S Novikov, T Sweeney, JE Robinson, SP Premaratne, B Suri, FC Wellstood, and BS Palmer. Raman coherence in a circuit quantum electrodynamics lambda system. *Nature Physics*, 12(1):75–79, 2016.

[72] Nissim Ofek, Andrei Petrenko, Reinier Heeres, Philip Reinhold, Zaki Leghtas, Brian Vlastakis, Yehan Liu, Luigi Frunzio, SM Girvin, L Jiang, et al. Extending the lifetime of a quantum bit with error correction in superconducting circuits. *Nature*, 536(7617): 441–445, 2016.

[73] W. D. Oliver. Mach-zehnder interferometry in a strongly driven superconducting qubit. *Science*, 310(5754):1653–1657, Dec 2005. ISSN 1095-9203. doi:10.1126/science.1119678. URL `http://dx.doi.org/10.1126/science.1119678`.

[74] Hanhee Paik, D. I. Schuster, Lev S. Bishop, G. Kirchmair, G. Catelani, A. P. Sears, B. R. Johnson, M. J. Reagor, L. Frunzio, L. I. Glazman, S. M. Girvin, M. H. Devoret, and R. J. Schoelkopf. Observation of high coherence in Josephson junction qubits measured in a three-dimensional circuit QED architecture. *Physical Review Letters*, 107(24):240501, 2011.

[75] Alex P. M. Place, Lila V. H. Rodgers, Pranav Mundada, Basil M. Smitham, Mattias Fitzpatrick, Zhaoqi Leng, Anjali Premkumar, Jacob Bryon, Sara Sussman, Guangming Cheng, Trisha Madhavan, Harshvardhan K. Babla, Berthold Jaeck, Andras Gyenis, Nan Yao, Robert J. Cava, Nathalie P. de Leon, and Andrew A. Houck. New material platform for superconducting transmon qubits with coherence times exceeding 0.3 milliseconds, 2020.

[76] Ioan M Pop, Kurtis Geerlings, Gianluigi Catelani, Robert J Schoelkopf, Leonid I Glazman, and Michel H Devoret. Coherent suppression of electromagnetic dissipation due to superconducting quasiparticles. *Nature*, 508(7496):369–372, 2014.

[77] Ioan-Mihai Pop, Benoît Douçot, L Ioffe, I Protopopov, Florent Lecocq, Iulian Matei, Olivier Buisson, and Wiebke Guichard. Experimental demonstration of aharonov-casher interference in a Josephson junction circuit. *Physical Review B*, 85(9):094503, 2012.

[78] John Preskill. Quantum computing in the NISQ era and beyond. *Quantum*, 2:79, 2018.

[79] John Preskill. Quantum computing 40 years later, 2023.

[80] E. M. Purcell, H. C. Torrey, and R. V. Pound. Resonance absorption by nuclear magnetic moments in a solid. *Phys. Rev.*, 69:37–38, Jan 1946. doi:10.1103/PhysRev.69.37. URL `https://link.aps.org/doi/10.1103/PhysRev.69.37`.

[81] MD Reed, BR Johnson, AA Houck, L DiCarlo, JM Chow, DI Schuster, L Frunzio, and RJ Schoelkopf. Fast reset and suppressing spontaneous emission of a superconducting qubit. *Applied Physics Letters*, 96(20):203110, 2010.

[82] Chad Rigetti, Jay M Gambetta, Stefano Poletto, BLT Plourde, Jerry M Chow, AD Córcoles, John A Smolin, Seth T Merkel, JR Rozen, George A Keefe, et al. Superconducting qubit in a waveguide cavity with a coherence time approaching 0.1 ms. *Physical Review B*, 86(10):100506, 2012.

[83] M. A. Rol, F. Battistel, F. K. Malinowski, C. C. Bultink, B. M. Tarasinski, R. Vollmer, N. Haider, N. Muthusubramanian, A. Bruno, B. M. Terhal, and L. DiCarlo. Fast, high-fidelity conditional-phase gate exploiting leakage interference in weakly anharmonic superconducting qubits. *Phys. Rev. Lett.*, 123:120502, Sep 2019. doi:10.1103/PhysRevLett.123.120502. URL `https://link.aps.org/doi/10.1103/PhysRevLett.123.120502`.

[84] Johannes A. Russer and Peter Russer. Lagrangian and hamiltonian formulations for classical and quantum circuits. *IFAC Proceedings Volumes*, 45(2):439–444, 2012. ISSN 1474-6670. doi:https://doi.org/10.3182/20120215-3-AT-3016.00077. URL `https://www.sciencedirect.com/science/article/pii/S1474667016307108`. 7th Vienna International Conference on Mathematical Modelling.

[85] Nicolas Schlosser, Georges Reymond, Igor Protsenko, and Philippe Grangier. Sub-poissonian loading of single atoms in a microscopic dipole trap. *Nature*, 411(6841): 1024–1027, 2001.

[86] RJ Schoelkopf, AA Clerk, SM Girvin, KW Lehnert, and MH Devoret. Qubits as spectrometers of quantum noise. In *Quantum noise in mesoscopic physics*, pages 175–203. Springer, 2003.

[87] Eyob A Sete, Matthew Reagor, Nicolas Didier, and Chad T Rigetti. Flatsonium: Charge and flux insensitive tunable superconducting qubit. *arXiv preprint arXiv:1703.04613*, 2017.

[88] Justin B Spring, Benjamin J Metcalf, Peter C Humphreys, W Steven Kolthammer, Xian-Min Jin, Marco Barbieri, Animesh Datta, Nicholas Thomas-Peter, Nathan K Langford, Dmytro Kundys, et al. Boson sampling on a photonic chip. *Science*, 339 (6121):798–801, 2013.

[89] Matthias Steffen, Shwetank Kumar, David P DiVincenzo, JR Rozen, George A Keefe, Mary Beth Rothwell, and Mark B Ketchen. High-coherence hybrid superconducting qubit. *Physical Review Letters*, 105(10):100502, 2010.

[90] Maika Takita, Antonio D Córcoles, Easwar Magesan, Baleegh Abdo, Markus Brink, Andrew Cross, Jerry M Chow, and Jay M Gambetta. Demonstration of weight-four parity measurements in the surface code architecture. *Physical Review Letters*, 117 (21):210505, 2016.

[91] R Versluis, S Poletto, N Khammassi, N Haider, DJ Michalak, A Bruno, K Bertels, and L DiCarlo. Scalable quantum circuit and control for a superconducting surface code. *arXiv preprint arXiv:1612.08208*, 2016.

[92] R. Vijay, D. H. Slichter, and I. Siddiqi. Observation of quantum jumps in a superconducting artificial atom. *Phys. Rev. Lett.*, 106:110502, Mar 2011. doi:10.1103/PhysRevLett.106.110502. URL `https://link.aps.org/doi/10.1103/PhysRevLett.106.110502`.

[93] D Vion, A Aassime, A Cottet, Pl Joyez, H Pothier, C Urbina, D Esteve, and Michel H Devoret. Manipulating the quantum state of an electrical circuit. *Science*, 296(5569): 886–889, 2002.

[94] U. Vool, A. Kou, W. C. Smith, N. E. Frattini, K. Serniak, P. Reinhold, I. M. Pop, S. Shankar, L. Frunzio, S. M. Girvin, and M. H. Devoret. Driving forbidden transitions in the fluxonium artificial atom. *Physical Review Applied*, 9(5):054046, 2018.

[95] Uri Vool, Ioan M Pop, Katrina Sliwa, Baleegh Abdo, Chen Wang, Teresa Brecht, Yvonne Y Gao, Shyam Shankar, Michael Hatridge, Gianluigi Catelani, et al. Non-poissonian quantum jumps of a fluxonium qubit due to quasiparticle excitations. *Physical review letters*, 113(24):247001, 2014.

[96] Andreas Wallraff, David I Schuster, Alexandre Blais, L Frunzio, R-S Huang, J Majer, S Kumar, Steven M Girvin, and Robert J Schoelkopf. Strong coupling of a single photon to a superconducting qubit using circuit quantum electrodynamics. *Nature*, 431(7005):162–167, 2004.

[97] Ken X Wei, Isaac Lauer, Srikanth Srinivasan, Neereja Sundaresan, Douglas T McClure, David Toyli, David C McKay, Jay M Gambetta, and Sarah Sheldon. Verifying multipartite entangled ghz states via multiple quantum coherences. *arXiv preprint arXiv:1905.05720*, 2019.

[98] D.K. Weiss, Helin Zhang, Chunyang Ding, Yuwei Ma, David I. Schuster, and Jens Koch. Fast high-fidelity gates for galvanically-coupled fluxonium qubits using strong flux modulation. *PRX Quantum*, 3:040336, Dec 2022. doi:10.1103/PRXQuantum.3.040336. URL `https://link.aps.org/doi/10.1103/PRXQuantum.3.040336`.

[99] Victor Frederick Weisskopf and Eugene Paul Wigner. Calculation of the natural brightness of spectral lines on the basis of dirac's theory. *Z. Phys.*, 63:54–73, 1930.

[100] Fei Yan, Simon Gustavsson, Archana Kamal, Jeffrey Birenbaum, Adam P Sears, David Hover, Ted J Gudmundsen, Danna Rosenberg, Gabriel Samach, Steven Weber, et al. The flux qubit revisited to enhance coherence and reproducibility. *Nature communications*, 7(1):1–9, 2016.

[101] Jian Q. You, Xuedong Hu, S Ashhab, and Franco Nori. Low-decoherence flux qubit. *Physical Review B*, 75(14):140515, 2007.

[102] Brian B Zhou, Alexandre Baksic, Hugo Ribeiro, Christopher G Yale, F Joseph Heremans, Paul C Jerger, Adrian Auer, Guido Burkard, Aashish A Clerk, and David D Awschalom. Accelerated quantum control using superadiabatic dynamics in a solid-state lambda system. *Nature Physics*, 13(4):330–334, 2017.

[103] Zhongyuan Zhou, Shih-I Chu, and Siyuan Han. Suppression of energy-relaxation-induced decoherence in λ-type three-level squid flux qubits: A dark-state approach. *Physical Review B*, 70(9):094513, 2004.

[104] Guanyu Zhu and Jens Koch. Asymptotic expressions for charge-matrix elements of the fluxonium circuit. *Physical Review B*, 87(14):144518, 2013.

[105] Guanyu Zhu, David G Ferguson, Vladimir E Manucharyan, and Jens Koch. Circuit QED with fluxonium qubits: Theory of the dispersive regime. *Physical Review B*, 87 (2):024510, 2013.